Advanced Hybrid Membranes for Next Generation PEMFC Automotive Applications.

Final Report

PI: Andrew M. Herring, Department of Chemical and Biological Engineering, Colorado School of Mines, Golden, CO 80401

Project Period: October 1st, 2013 – July 31st, 2017
Date of Report: March 1tst 2018

Recipient: Colorado School of Mines
Award Number: DE-EE0006363

Working Partners: CSM: Andrew R. Motz, Mei-Chen Kuo, James L. Horan, Jessica Hoffman, Yating Yang, Tara P. Pandey.
Cost-Sharing Partners: 3M: Michael Yandrasits, Consultant: Steven J. Hamrock, Nissan Technical Center North America, Nilesh Dale, Ramesh Yadav, NREL: Bryan Pivovar, Michael Penner, Guido Bender

Contact: Andrew M. Herring
Tel: (303) 384-2082
Email: aherring@mines.edu

DOE Managers: Donna Ho, Gregory Kleen

Acknowledgment: This material is based upon work supported by the Department of Energy's Office of Energy Efficiency and Renewable Energy (EERE) under the Fuel Cell Technology Office Award Number DE-EE0006363.

Table of Contents

1. Project Objective

The objective of this proposal is to fabricate a low cost high performance hybrid inorganic/polymer membrane that has a proton area specific resistance (ASR) < 0.02 ohm cm^2 at the operating temperature of an automotive fuel cell stack (95 - 120°C) at low inlet RH <50% with good mechanical and chemical durability. Additionally the membrane will be optimized for low hydrogen and oxygen crossover with high electrical ASR at all temperatures and adequate proton ASR at lower temperatures. We also seek to gain valuable insights into rapid proton transport at the limit of proton hydration. Additional research will be performed to incorporate the membrane into a 50 cm^2 membrane electrode assembly (MEA). The materials at the start of this project are at a TRL of 2, as we have shown that they have proton conductivity under high and dry conditions, but we have not yet consistently shown that they will function in an operational fuel cell. At the project's end the materials will be at a TRL of 4 and will be integrated into an MEA, demonstrating that they can function with electrodes as a single fuel cell.

2. Background

In past funding from the DOE/NSF we have developed completely new ionomer systems based on incorporation of inorganic super acids into polymer systems, which have high proton conductivity under conditions of low humidity, higher temperature operation, high oxidative stability, and little swelling when wet. This project will perform the work to optimize the proton conductivity and mechanical properties in these materials to produce a robust thin film for PEM fuel cells in automotive applications. The technical concept is to use functionalized inorganic super acids that utilize little water for high proton conductivity, as the protogenic group covalently attached to a polymer backbone optimized for all other functions of the membrane. Many composite inorganic/polymer films have been fabricated, but unless the particles have dimensions on the nano-scale there is no advantage as the improvement to film properties occurs at the particle polymer interface. The limit of this approach is to use molecules with high acidity as the highly activating functionalities, but to do this we must immobilize them, control the morphology of the proton conducting channel, and fabricate an amorphous material. The two moieties that have received the most attention and appear to greatly enhance proton transport are heteropoly acids (HPAs) and Zirconyl phosphonates (ZrPs). In previous work, we demonstrated both composite membranes and true inorganic/polymer hybrid materials with very high proton conductivity, but the inorganic super acid in the membrane was not immobilized and the inorganic/polymer hybrid material transformed into undesirable crystalline phases at low RH. These materials are not yet fuel cell ready. In this project, we will overcome all of these disadvantages with an innovative approach to amorphous materials to produce high proton conductivity and all other properties desired of a PEM.

The project is addressing the 2017 DOE technical targets for membranes for transportation applications. At the core of this effort is the development of a membrane with an ASR of 0.02 □Ω□cm^2 at 80 °C and at the maximum operating temperature of the envisioned fuel cell stack at low partial pressures of water (p_{H2O} 25 kPa at 80°C, 40 kPa at 120°C). Cross over of 2 mA cm^{-2} for hydrogen and oxygen and a minimum electrical resistance of 1,000 Ω cm^2 will be achieved. In addition, the film will survive 20,000 cycles of the DOE mechanical test and >500 hours of the chemical crossover test.

3. Market, Environmental, and Energy Benefit Analysis (NREL)
Several studies report on the potential impact of fuel cell systems from an environmental and energy impact the high temperature fuel cell membrane technologies being developed will likely have minor impact compared to baseline fuel cell systems in the areas of environmental or energy impact (although slight improvements in efficiency may be possible due to increased cell efficiency) and baseline analysis for fuel cell system deployment in these areas are referenced. The primary issue for the technology being developed is in improved market penetration due to improved economics of the developed systems. In order to evaluate the potential gains in technology, system economics have been compared using DOE funded baseline work (Brian James, Strategic Analysis Inc. **http://www1.eere.energy.gov/hydrogenandfuelcells/pdfs/sa_fc_system_cost_analysis_2012.pdf**) in Table 1, we report a comparison of baseline fuel cell systems compared to HT-PEM systems developed based on advanced materials projected from this project, variables investigated in this analysis are highlighted specifically in the Table. The model analysis submitted has several assumptions: the new materials will allow for operation up to 120C (there by increasing the heat rejection capability of the system and lowering the radiator size); the system humidification system can be removed due to the increased conductivity under dry conditions of the membrane materials; and the increased operating temperature will allow for catalytic gains (in this case we allowed for decreased catalyst loading; however increased cell performance could also be considered). We also assumed the membrane materials would be slightly (20%) more expensive than baseline materials.

Specification	UOM	Baseline	HT-PEM
Current density	A/cm^2	1.456	1.456
Voltage	Vdc	0.676	0.676
Relative waste heat rejection		100%	100%
Relative stack area		100%	1
Relative fuel efficiency		100%	1.000
Relative fuel storage		100%	1.000
Stack temperature	°C	87	120
Maximum ambient temperature	°C	40	40
Maximum ambient dT	°C	47	80
Cooling system capacity		100%	59%
Number of subsystems for assembly		10	8
Total Pt loading	mgPt/cm^2	0.186	0.1395
Relative membrane cost		100%	120%
Relative GDL cost		100%	100%
Relative bipolar plate cost		100%	100%

Table 2 shows projections of cost per automotive system based on these changes (black numbers denote no change to baseline projections, green numbers denote a decreased cost relative to baseline, and red numbers denote an increased cost relative to baseline). The material advance has led to a decrease cost in the stack, balance of plant and system costs. Perhaps the most relevant impact is on projected high volume production costs where the projection for 500,000 vehicle production level has been decreased by more than $500/system to a total system cost of $3231.93 or a cost projection of $40.40/kWnet. This value is significantly lower than the baseline ($46.95/kWnet) and will improve the market competitiveness of fuel cell automotive systems.

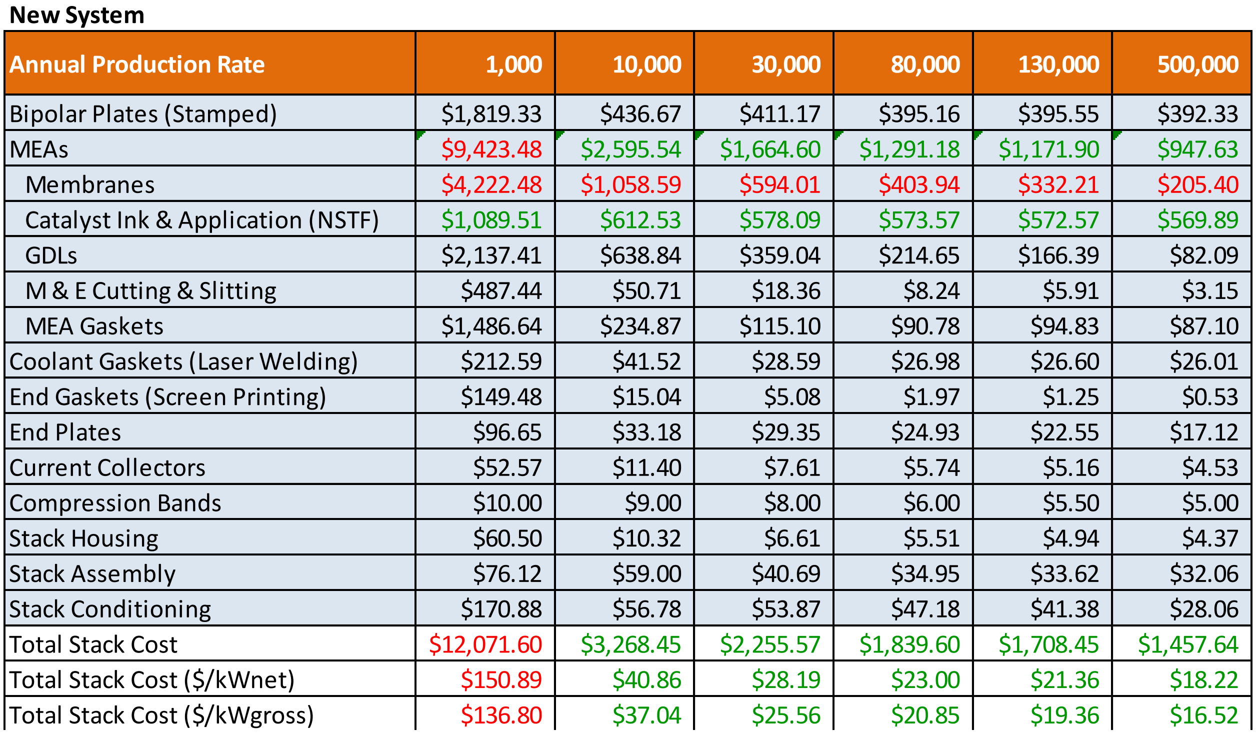

New System

Annual Production Rate	1,000	10,000	30,000	80,000	130,000	500,000
Bipolar Plates (Stamped)	$1,819.33	$436.67	$411.17	$395.16	$395.55	$392.33
MEAs	$9,423.48	$2,595.54	$1,664.60	$1,291.18	$1,171.90	$947.63
Membranes	$4,222.48	$1,058.59	$594.01	$403.94	$332.21	$205.40
Catalyst Ink & Application (NSTF)	$1,089.51	$612.53	$578.09	$573.57	$572.57	$569.89
GDLs	$2,137.41	$638.84	$359.04	$214.65	$166.39	$82.09
M & E Cutting & Slitting	$487.44	$50.71	$18.36	$8.24	$5.91	$3.15
MEA Gaskets	$1,486.64	$234.87	$115.10	$90.78	$94.83	$87.10
Coolant Gaskets (Laser Welding)	$212.59	$41.52	$28.59	$26.98	$26.60	$26.01
End Gaskets (Screen Printing)	$149.48	$15.04	$5.08	$1.97	$1.25	$0.53
End Plates	$96.65	$33.18	$29.35	$24.93	$22.55	$17.12
Current Collectors	$52.57	$11.40	$7.61	$5.74	$5.16	$4.53
Compression Bands	$10.00	$9.00	$8.00	$6.00	$5.50	$5.00
Stack Housing	$60.50	$10.32	$6.61	$5.51	$4.94	$4.37
Stack Assembly	$76.12	$59.00	$40.69	$34.95	$33.62	$32.06
Stack Conditioning	$170.88	$56.78	$53.87	$47.18	$41.38	$28.06
Total Stack Cost	$12,071.60	$3,268.45	$2,255.57	$1,839.60	$1,708.45	$1,457.64
Total Stack Cost ($/kWnet)	$150.89	$40.86	$28.19	$23.00	$21.36	$18.22
Total Stack Cost ($/kWgross)	$136.80	$37.04	$25.56	$20.85	$19.36	$16.52

New System

Annual Production Rate	1,000	10,000	30,000	80,000	130,000	500,000

Air Loop	$1,736.16	$1,039.80	$1,038.41	$897.04	$869.19	$842.01
Humidifier and Water Recovery Loop	$0.00	$0.00	$0.00	$0.00	$0.00	$0.00
High-Temperature Coolant Loop	$390.32	$335.74	$335.60	$294.45	$278.59	$259.16
Low-Temperature Coolant Loop	$0.00	$0.00	$0.00	$0.00	$0.00	$0.00
Fuel Loop	$348.71	$303.32	$293.76	$263.92	$253.63	$240.38
System Controller	$136.86	$120.43	$109.48	$82.11	$76.64	$65.69
Sensors	$1,365.32	$714.40	$714.40	$527.97	$434.76	$180.39
Miscellaneous	$229.11	$133.30	$126.30	$115.40	$111.54	$108.06
Total BOP Cost	$4,206.48	$2,646.99	$2,617.95	$2,180.89	$2,024.35	$1,695.69
Total BOP Cost ($/kWnet)	$52.58	$33.09	$32.72	$27.26	$25.30	$21.20
Total BOP Cost ($/kWgross)	$47.67	$30.00	$29.67	$24.72	$22.94	$19.22

Fuel Cell Stacks	$12,071.60	$3,268.45	$2,255.57	$1,839.60	$1,708.45	$1,457.64
Balance of Plant	$4,206.48	$2,646.99	$2,617.95	$2,180.89	$2,024.35	$1,695.69
System Assembly & Testing	$116.10	$80.50	$79.12	$78.95	$78.59	$78.60
Total System Cost ($)	$16,394.18	$5,995.93	$4,952.64	$4,099.44	$3,811.39	$3,231.93
Total System Cost ($/kWnet)	$204.93	$74.95	$61.91	$51.24	$47.64	$40.40
Total System Cost ($/kWgross)	$185.79	$67.95	$56.13	$46.46	$43.19	$36.63
Differential						
Fuel Cell Stacks ($/vehicle)	$340.58	($27.75)	($93.69)	($123.86)	($135.50)	($155.72)
Balance of Plant ($/vehicle)	($1,321.19)	($681.29)	($602.84)	($490.45)	($444.03)	($348.88)
System Assembly & Testing ($/vehicl	($29.03)	($20.12)	($19.78)	($19.74)	($19.65)	($19.65)

For employment impacts see reference:
http://www.hydrogen.energy.gov/pdfs/review13/an035_mintz_2013_o.pdf
For environmental impacts see reference:
http://www.hydrogen.energy.gov/pdfs/review12/an_plenary_joseck_2012_o.pdf

4. Optimization of polyZrP Membranes based on Zirconyl phosphonates, polyZrP

A common theme in this project was the use of inorganic super acid moieties fuctionalized with organic polymerizable groups. We had previously discovered a highly proton conducting polymer based on the co-polymerization of zirconyl phosphonate with vinylphosphonic acid (VPA) that had very high proton conductivity.[1] So this materials was one of the three candidate platforms that we chose to study.

4.1 Experimental

Zirconyl chloride octahydrate, $ZrOCl_2.8H_2O$(Aldrich, 224316, 98%)
Vinylphosphonic acid, $(CH_2{=}CHP(O)(OH)_2$, (Aldrich, 67206-8, ≥ 90.0%)
2-Hydroxy-2-methylpropiophenone, $C_6H_5COC(CH_3)_2OH$, (Aldrich, 405655, 97%)

Zirconyl chloride octahydrate ($ZrOCl_2.8H_2O$, 24.5 g, 74.51 mmol) in DI water (160 mL) was slowly added to the clear solution of vinylphosphonic acid (VPA, 24g, 199.95 mmol) in DI water (100 mL) with stirring. A white precipitate formed immediately. The reaction mixture was refluxed at 60 °C for 5 days. The resulting solid was collected on filter funnel. The solid product was washed with water, acetone, and diethyl ether, then air dried. Yield: 25.5 g.

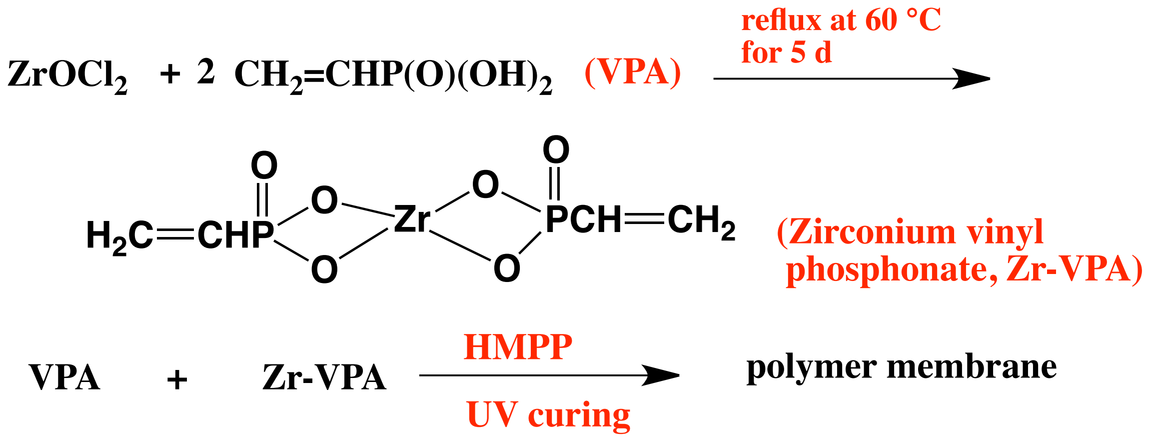

Figure 1.Preparation of Zr-VPA and polymerization with VPA under UV curing.

We polymerized Zr-VPA with VPA using a UV and an initiator, HMPP. The general procedure was shown in Scheme 1 above. Zr-VPA (1g, 20% wt) and VPA (4.4 g, 90% pure, 80 % wt) was mixed at room temperature. VPA is clear liquid at room temperature, with a purity of 90%, and the 10% of components in water. Water is able to increase the mobility of the monomers. The suspension was purged with nitrogen gas, sealed in a glass vial, and sonicated for 20 min. The suspension was stayed overnight at room temperature. HMPP (UV initiator, 5% of total weight) was added to the reaction mixture and sonicated for 20 min. This reaction mixture was casted in between silicon-treated Mylar sheets, which were on a glass plate. The mixture was passed through a F300 Series Fusion UV curing system 20 times at 12 ft/min under a P300mT power supply corresponding to a power of 300 W/in.

4.2 Results

The membrane was a clear pale yellow film.

The thickness for Zr-VPA membrane was 149 µm. The Area specific resistance (ASR) measurement was shown in Figure 1.

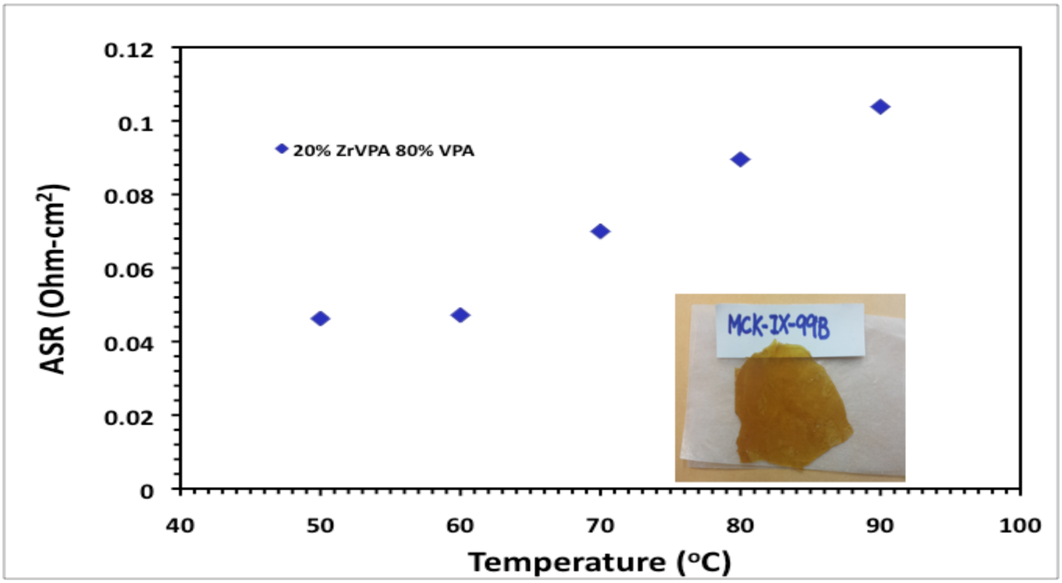

Figure 2. ASR for a typical Zr-VPA Membrane (20% Zr-VPA , 80% VPA)

To achieve the DOE ASR target of 0.02 Ωcm^2 the film would need to be <97 µm. Unfortunately, despite many attempts we could not make a water stable film with this chemistry and so the approach was abandoned. The issue seems to be with the time of mixing of the zirconyl vinyl phosphonate with the vinyl phosphonic acid, which gives very different results on the quality of the final polymer film.

5. Optimization of poly-HPA-tetrafluorovinylether (TFVE) Membranes

The second approach to make a hybrid polymer containing a super-acid moiety was to make a monomer of a heteropoly acid. This approach was used successfully in a previously funded effort, where model materials based on divinyl HPA monomers where made using acrylate chemistry.[2] The membranes from the acrylate approach demonstrated conductivities >0.1 S cm^{-1} at 50%RH and temperatures >90°C.[3] The model system was not deemed practical for fuel cell systems as it was thought that the ester linkage would be susceptible to hydrolysis. So we modified the approach to make a perfluorinated materials using tetrafluoro vinylether (TFVE) chemistry. When TFVEs are heated they combine to make perflorinated cyclobutanes and so can this approach can be used to make perfluoriated polymers. The first step though is to have very pure monomers, as any molecules with hydrogen substitution greatly reduce the obtainable molecular weight.

5.1 Experimental

Fluoroalkylation of 4-bromophenol to give the dibromo intermediate I is followed by activated Zn-mediated elimination to gave the trifluorovinyl ether compound II by standard procedures.[4,5] The only significant side reaction during fluoroalkylation was protonation of an intermediated tetrafluoroethyl ether anion-presumably by adventitious water-giving a small quantity of tetrafluoroethyl ether (Ar-OCF_2CF_2H). This troublesome impurity functions as a terminating agent if not removed and therefore limits the molecular weight during subsequent step growth cyclopolymerization. The byproduct (Ar-OCF_2CF_2H) was more effectively removed after elimination to aryl TFVE-Br by flashing over neutral alumina in hexane. The synthesis scheme of aryl TFVE-Br was shown in Figure 3. Treatment of TFVE-Br with Mg powder in the presence of chlorotriethylsilane, *in situ* Grignard formation and substitution was given in good yield. (see

Figure 4)

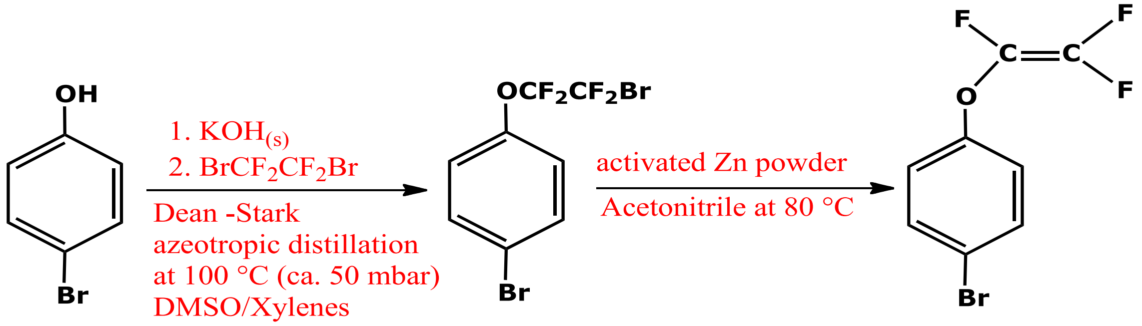

Compound I

TFVE-Br

Figure 3. Synthesis of aryl TFVE-Br.

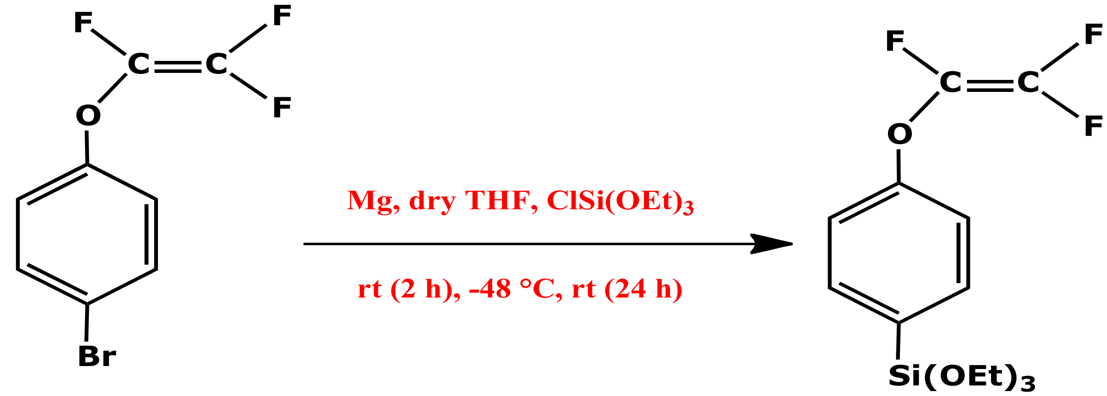

TFVE-Br **TFVE-Si(OEt)$_3$**

Figure 4. Synthesis of TFVE-Si(OEt)$_3$

Synthesis of TFVE-Si(OEt)$_3$[6]

The starting material is 1-bromo-4(trifluorovinyloxy) benzene (aryl TFVE-Br) from Oakwood Products, Inc. The price for aryl TFVE-Br is very expensive ($185/1g). We purchased the first 10 g of ρ-bromophenyl-TFVE but then we obtained the ability to synthesize this starting material (aryl TFVE-Br) in our lab. Aryl TFVE-Br was prepared in a two step process starting from phenolic precursor, 4-bromophenol, via alkylation with 1,2-dibromotetrafluorethane, followed by zinc mediated dehalogenation of the brominated intermediate (Compound I). The synthetic scheme is shown in Figure 3.[4,5] The NMR spectra were shown in

Figure 5 . The by-product (Ar-OCF$_2$CF$_2$H) could easily be detected with ^{1}H NMR because of the characteristic three triplet at δ 5.5-6.3 ppm. Aryl trifluorovinyl ether compounds are useful as monomers which undergo thermal cyclopolymerization to afford a new class of thermally stable perfluorocyclobutane (PFCB) aromatic polyethers.

Aryl TFVE-Br (0.1 mol) was added dropwise to a mixture of Mg powder (0.11 mol) and dry THF (250 mL). After complete addition, the reaction mixture was stirred for an additional 2 h at room temperature. Then, the reaction mixture was cooled down to -48 °C by using a dry ice/acetonitrile bath. Triethoxychlorosilane (ClSi(OEt)$_3$, 0.095 mol) was added dropwise while maintaining the reaction temperature at -48 °C. After addition, the reaction temperature was warmed to room temperature slowly and stirred at room temperature for 24 h. Then, the reaction mixture was poured into heptane and stirred at room temperature for 1 h. The solution was filtered to remove magnesium salt (MgBrCl) and evaporated the solvent on a rotary evaporator. The crude product was purified by silica gel (200-400 mesh) column chromatography using hexanes-EtOAc (ethyl acetate) (85:15) as the eluent to give clear pale yellow oil. Yield: 75%. The NMR spectrum was shown in Figure 6.

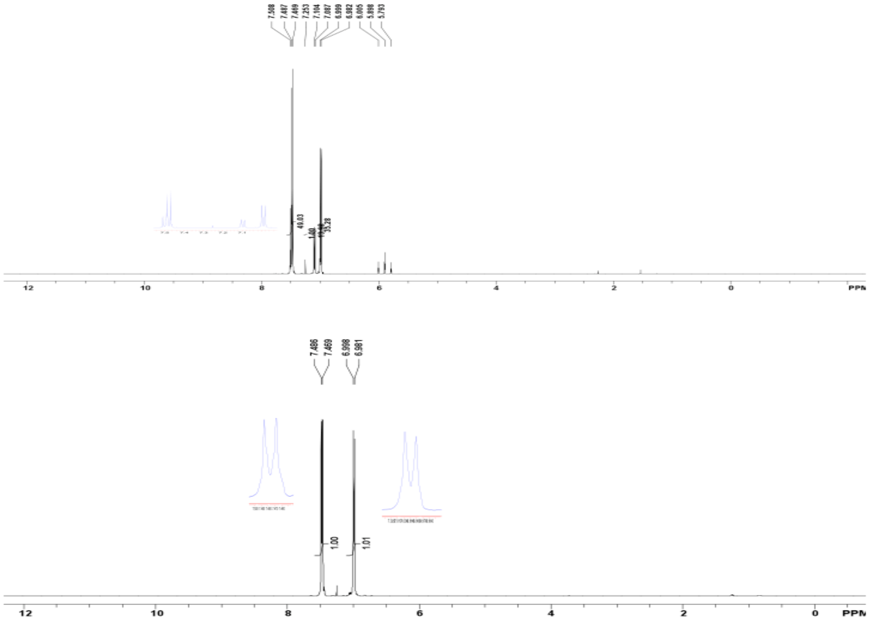

Figure 5. ^{1}H NMR spectra for aryl TFVE-Br (before and after purification).

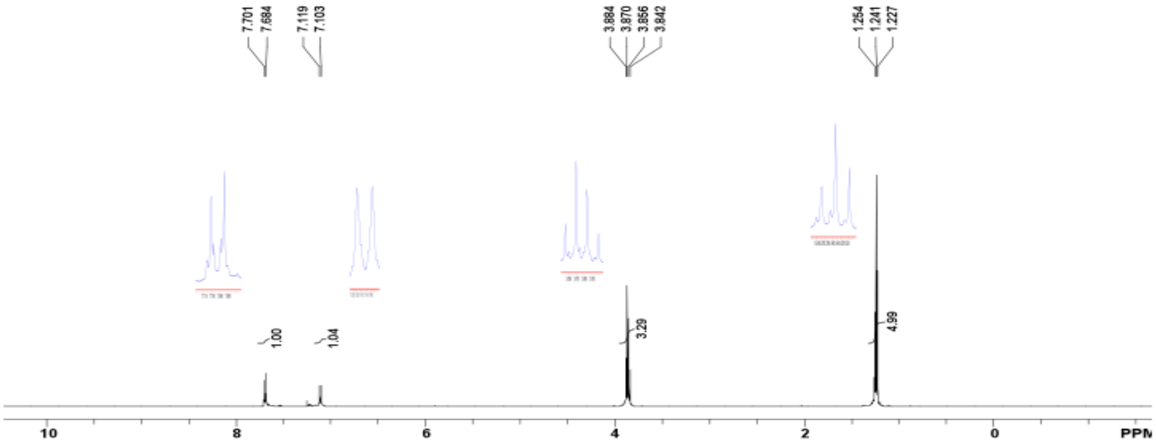

Figure 6. ^{1}H NMR spectrum for aryl TFVE-Si(OEt)$_3$.

<u>Synthesis of SiW$_{11}$O$_{39}$[(TFVE-Si)$_2$O]</u>

A silane-coupling agent (<u>TFVE-Si(OEt)</u>$_3$, 1.3546 g, 4 mmol) was added to 320 mL of a CH_3CN/ H_2O mixture(240/80, v/v). After stirring for 5 min (pH= 2.93 at 15.1 °C), solid K$_8$[α-SiW$_{11}$O$_{39}$].12H$_2$O (6.025 g, 2 mmol) was added slowly to the reaction mixture, followed by stirring for 5 min at room temperature (pH = 4.86 at 15.6 °C). The pH of the reaction mixture was adjusted to 1.8 with 1 M aqueous HCl solution. Total amount of 1 M HCl solution was 9.5 mL. The reaction mixture was changed to clear solution. The clear solution was stirred overnight at room temperature. A white precipitate formed in the suspension after stirring overnight. The reaction mixture was filtered with a membrane filter. The clear colorless filtrate was evaporated using a rotary evaporator at bath temperature 40 °C. The pale yellow power was dried in air after evaporation with a rotary evaporator. The crude product is [α-$SiW_{11}O_{39}(C_6H_4OCF{=}CF_2\text{-}Si)_2O]^{4-}$ (K^+ form, $KSiW_{11}O_{39}[(TFVE\text{-}Si)_2O]$. Yield: 6.85 g (98.3%). The H^+ form hybrid will be obtained with ion-change column. A strong stretching mode in the infrared at 1040 cm^{-1} (K^+ form) 1038 cm^{-1} (H^+ form) attributed to an Si-O-Si stretch. ^1H NMR (300 MHz, CD_3CN): δ, ppm: 7.2 (d, 2H), 7.7 (d, 2H).

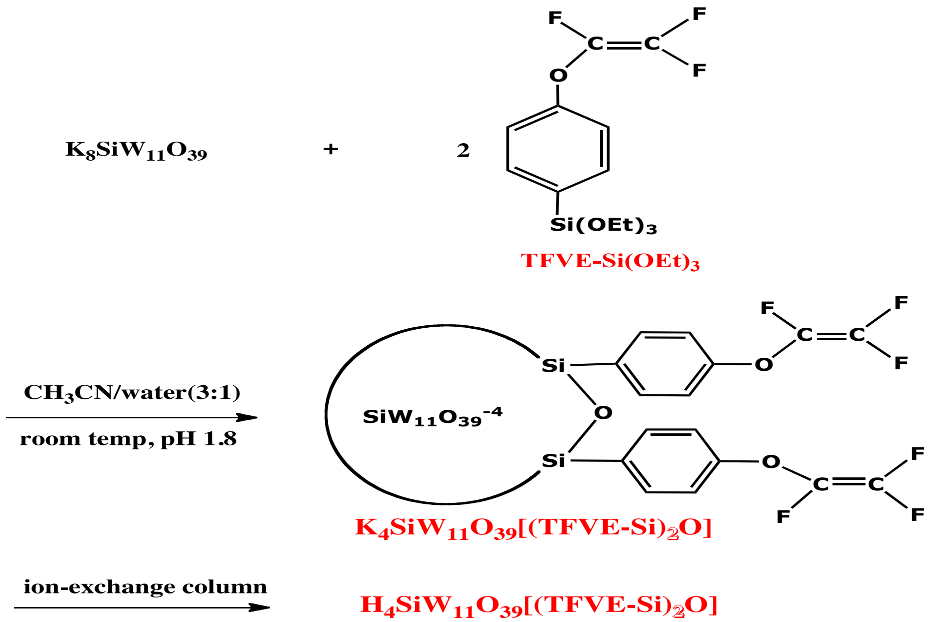

Figure 7. Synthesis of TFVE monomer-$SiW_{11}O_{39}[(TFVE\text{-}Si)_2O]$.

Two approaches were taken one to perform the polymerization in the presence of PVDF-HFP (poly(vinylidenefluoride-co-hexafluoropropene)), Figure 8, or to co-polymerize with different TFVE co-monomers, Figure 9, to make strong films. Unfortunately non of the blended films had good enough proton-conductivity to allow us to approach the DOE ASR targets. Non of the co-polymers that we synthesized formed films with good mechanical properties despite using long polymerization times at high temperatures and switching to high boiling solvents.

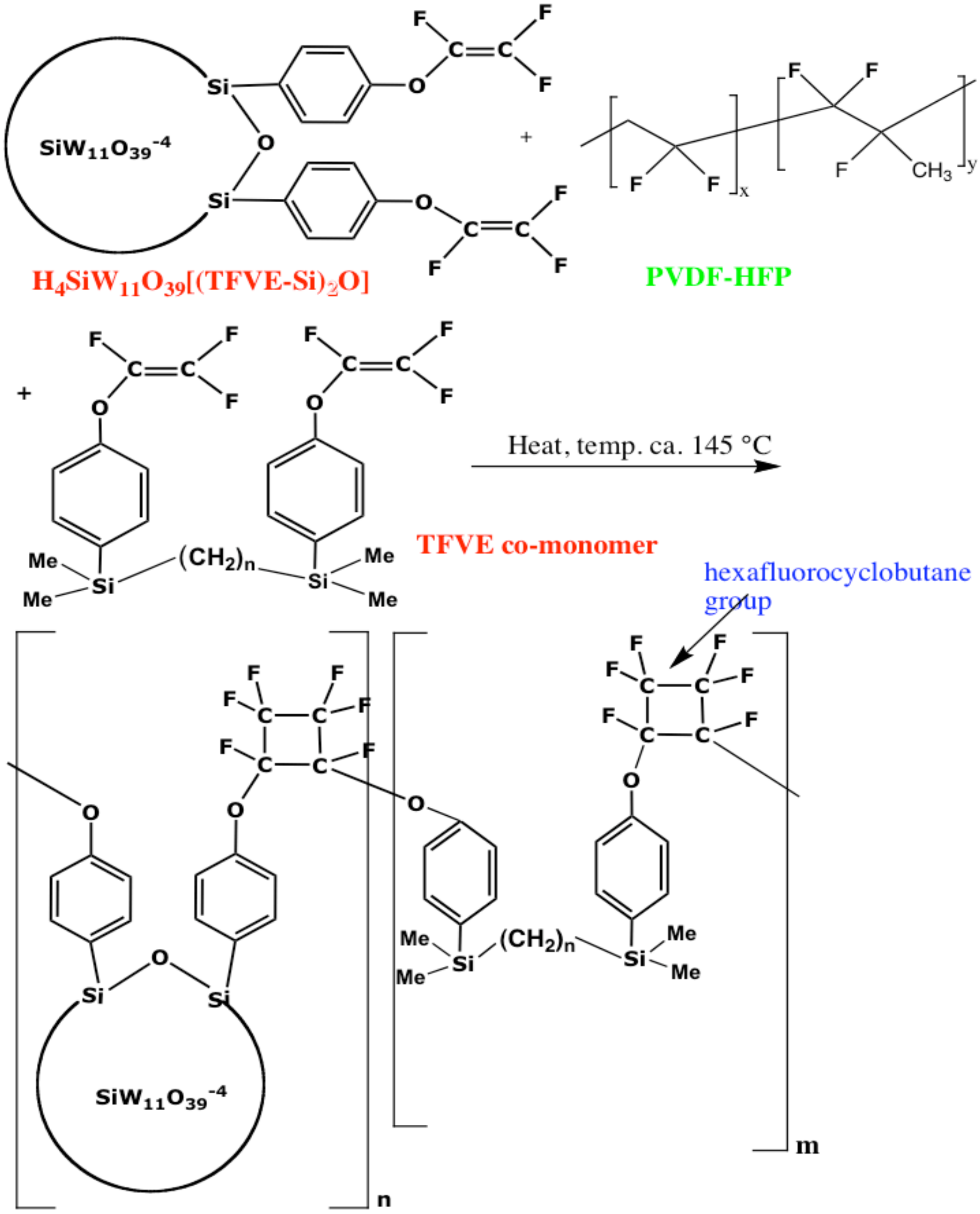

Figure 8. Polymerization scheme for $SiW_{11}O_{39}[(TFVE\text{-}Si)_2O]$.

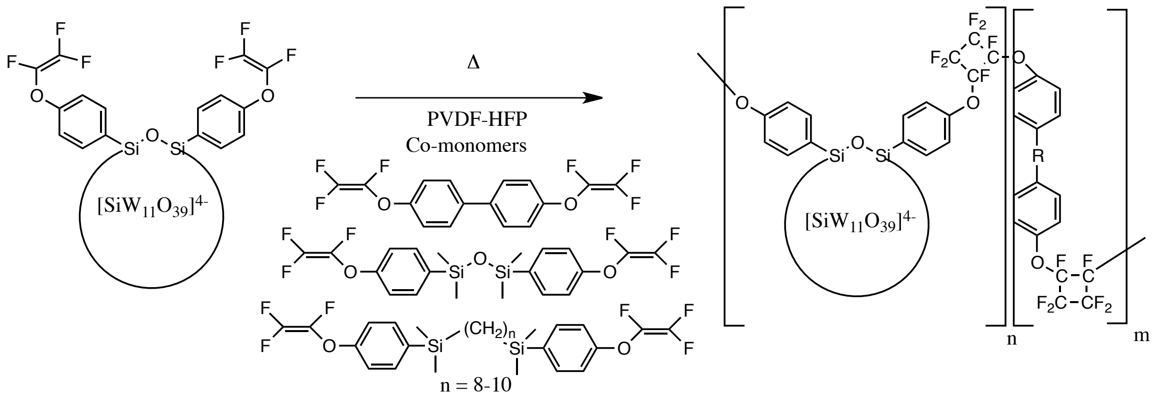

Figure 9. TFVE-HPA and co-monomer overall reaction scheme.

However, we encountered further problems with purifying materials in this synthetic program. We reported before that there was a byproduct in the synthesis of 4-(2-bromotetrafluoroethoxy) bromobenzene ($BrArOCF_2CF_2Br$). The byproduct was analyzed by ^1H NMR and determined to be bromotetrafluoroethyl ether ($BrArOCF_2CF_2H$). We encountered some difficulties to separate these two compounds because of the similarity of the fluorocarbon structures. The following synthesis was using this impure $BrArOCF_2CF_2Br$ and we again found the existence of $BrArOCF_2CF_2H$ in the synthesis of 4-[(trifluorovinyl)oxy]bromobenzene ($BrArOCF{=}CF_2$). The existence of $BrArOCF_2CF_2H$ was proved by ^1H NMR spectrum (Figure 10) and GC-MS (Figure 11). The four sets of doublets proved that there were two kinds of para- substituted benzene rings from two different compounds. From the integration of the peaks we knew that the impurities was about 15 %. Then we used GC-MS to confirm the structure of the impurity. The two peaks at different retention time proved there were two compounds. The m/z ratio for the two peaks was 252 and 274, respectively. The m/z ratio of 252 corresponds to $BrArOCF{=}CF_2$ and m/z ratio of 274 corresponds to $BrArOCF_2CF_2H$. We also confirmed the percentage of the $BrArOCF_2CF_2H$ to be 15 % through the integration of the GC/MS peaks.

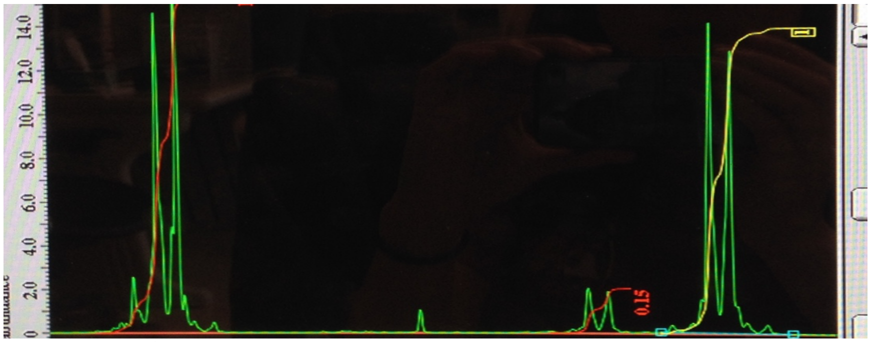

Figure 10. ^1H NMR spectrum of impure $BrArOCF{=}CF_2$.

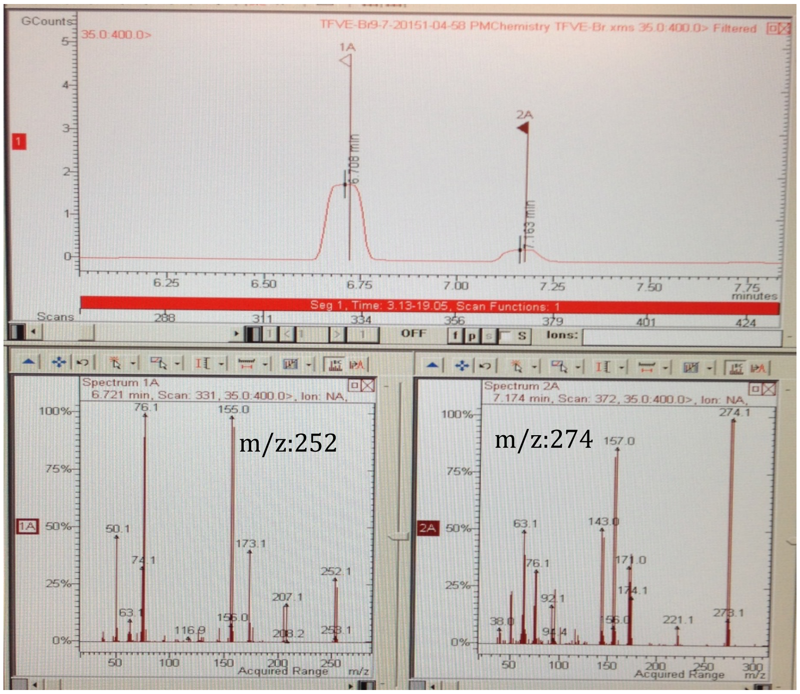

Figure 11. GC-MS spectrum of impure BrArOCF=CF$_2$.

Due to the similar reactivity of the two compounds, they can both conduct the following Grignard reaction (Figure 12) and then the impurity could lead to three different kinds of products, therefore limiting the molecular weight of the desired polymer. The three products are listed in Figure 13.

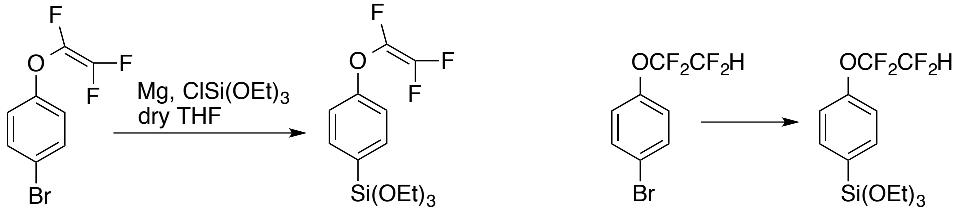

Figure 12: Grignard reaction of BrArOCF=CF$_2$ and BrArOCF$_2$CF$_2$H

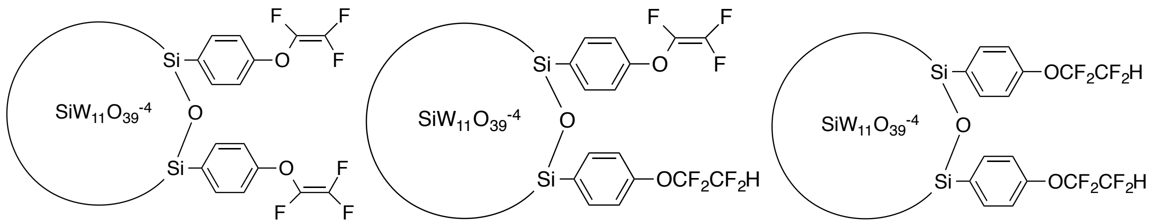

Figure 13: Possible monomer structures when using impure BrArOCF=CF$_2$.

Several different purification methods were tried to obtain pure BrArOCF=CF$_2$ and column chromatography was found to be the best way to get pure product. We also tried pure eluents and mixed eluents for the column chromatography. Pure hexane was chosen to separate BrArOCF=CF$_2$ from BrArOCF$_2$CF$_2$H. We performed ^{1}H NMR and GC-MS to characterize the separated compound. Figure 14 shows the ^{1}H NMR spectrum of the purified $BrArOCF=CF_2$ from column chromatography. The presence of two sets of doublets indicated the existence of one kind of para- substituted benzene ring that came from one compound.

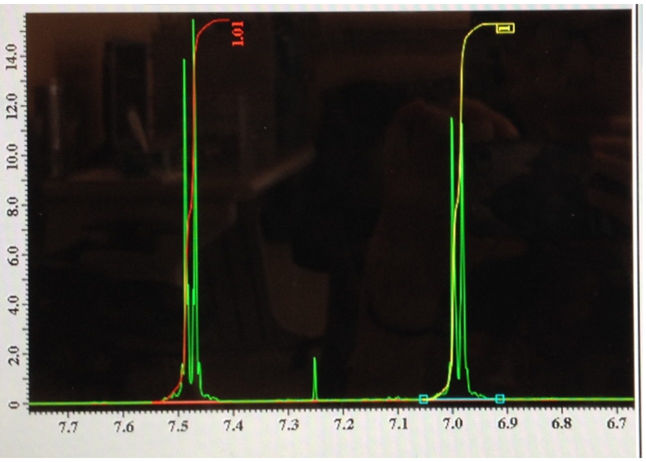

Figure 14. ^{1}H NMR spectrum of the purified $BrArOCF=CF_2$ in $CDCl_3$.

Figure 15 shows the comparison of GC-MS spectra of purified $BrArOCF=CF_2$ (top) and impure $BrArOCF=CF_2$ (bottom). The bottom spectrum have two peaks corresponding to $BrArOCF=CF_2$ (85 %) and $BrArOCF_2CF_2H$ (15 %). The top spectrum contains only one peak with m/z ratio of 252, indicating $BrArOCF=CF_2$ was the only compound after purification.

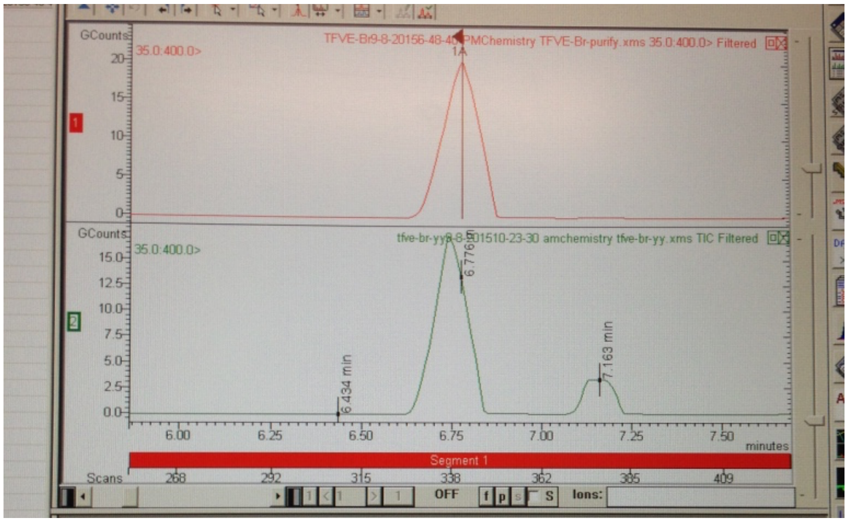

Figure 15. GC-MS spectra of purified $BrArOCF=CF_2$ (top) and impure $BrArOCF=CF_2$ (bottom).

The following synthesis of 4-[(trifluorovinyl)oxy]phenyltriethoxysilane (TFVE-$Si(OEt)_3$) was conducted through Grignard reaction. The structure and the purity of TFVE-$Si(OEt)_3$ were confirmed by ^{1}H NMR (Figure 16) and GC-MS (Figure 17) spectra.

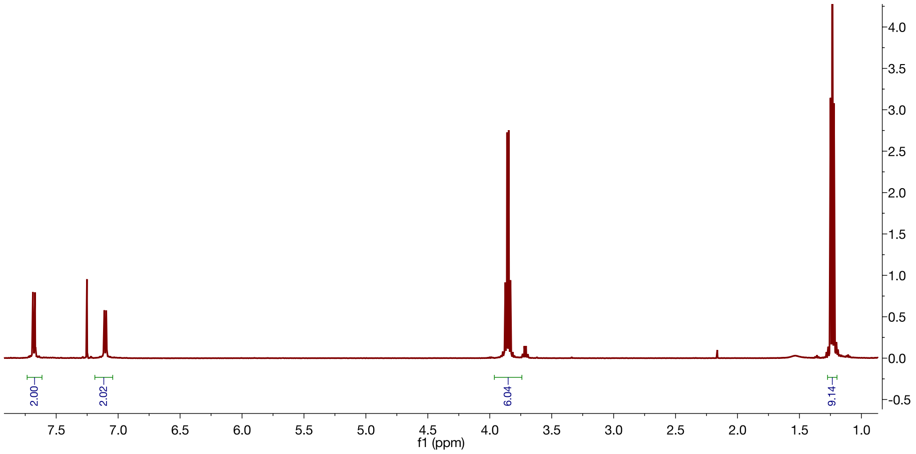

Figure 16. ^1H NMR spectrum of TFVE-Si(OEt)$_3$.

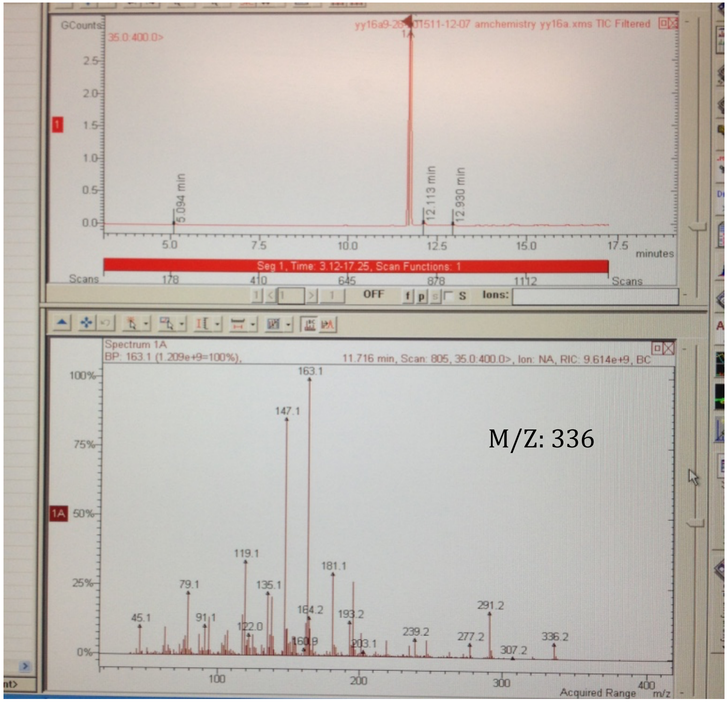

Figure 17. GC-MS spectrum of TFVE-Si(OEt)$_3$.

The attachment of heteropolyacid (HPA) to TFVE was conducted in a mixture of acetonitrile and water under acidic environment. The successful synthesis of TFVE-HPA was confirmed by FT-IR (Figure 18). The absorbance at 1833 cm^{-1} indicated the existence of CF=CF$_2$ bond and the absorbance at 1039 cm^{-1} indicated the existence of Si-O-Si bond.

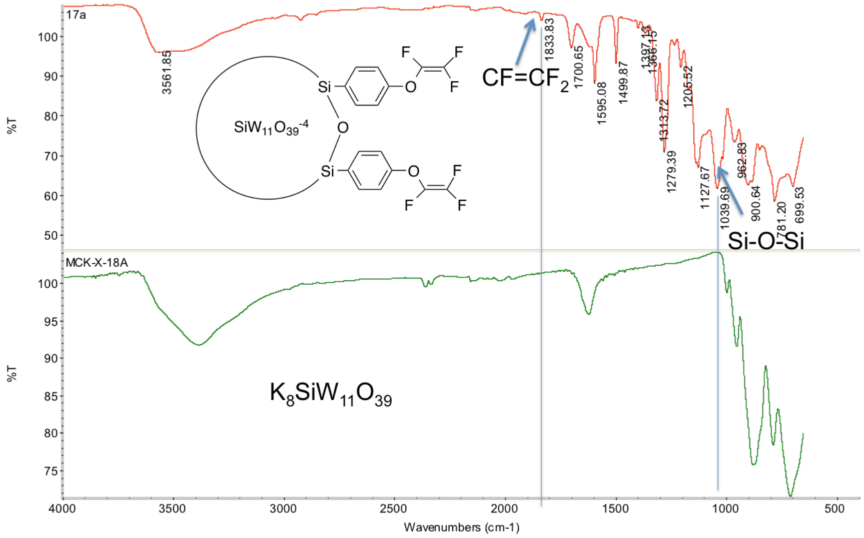

Figure 18. FT-IR spectra comparison of TFVE-HPA (top) and HPA (bottom).

Homopolymerization of TFVE-biphenol was studied to investigate the polymerization condition of TFVE polymerization (Figure 19). We received some TFVE-biphenol from 3M and did purity check on it. ^{1}H NMR (Figure 20, top) and ^{19}F NMR (Figure 20, bottom) spectra show the existence of impurities in TFVE-biphenol. The impurities peaks are the ones in the blue boxes.

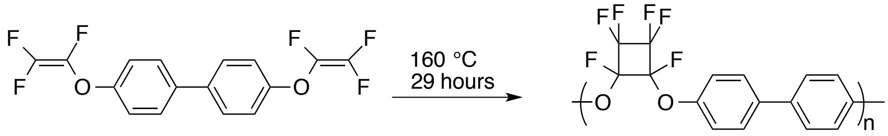

Figure 19: Homopolymerization of TFVE-biphenol.

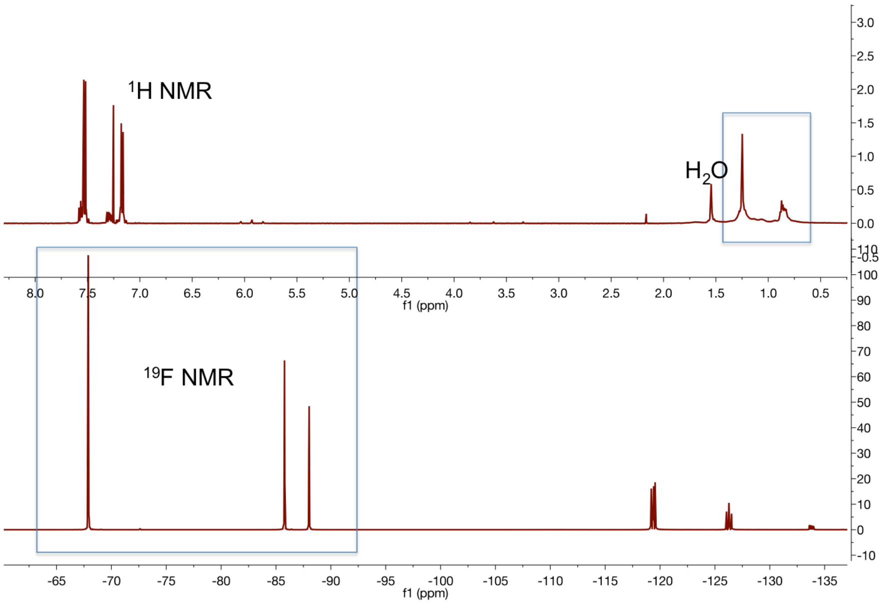

Figure 20. ^{1}H NMR (top) and ^{19}F NMR (bottom) of TFVE-biphenol from 3M.

Procedures were taken to purify TFVE-biphenol in order to synthesize high molecular weight homopolymer. The crude solid was recrystallized from ethanol/water mixture. The structure and purity of the purified TFVE-biphenol was confirmed with ^{1}H NMR (Figure 21, top) and ^{19}F NMR (Figure 21, bottom) spectra. The impurities peaks from the crude product were successfully eliminated in the purified TFVE-biphenol.

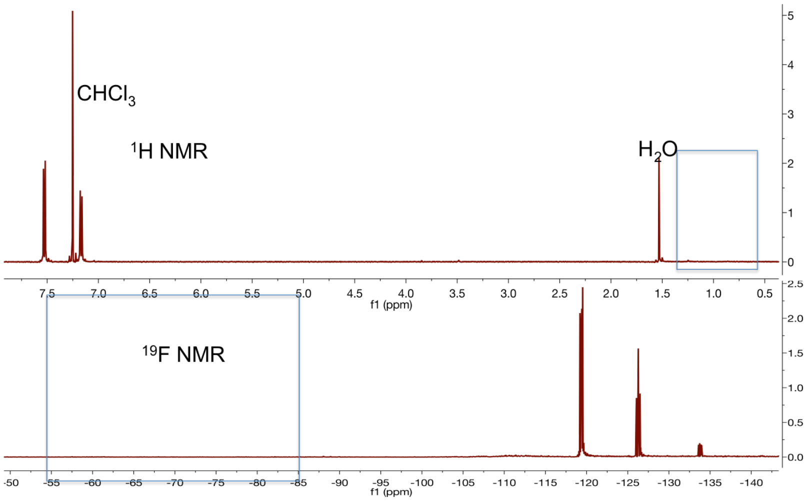

Figure 21. ^{1}H NMR (top) and ^{19}F NMR (bottom) of purified TFVE-biphenol.

Homopolymerization was carried out with the purified TFVE-biphenol to study the polymerization condition. Original attempts were conducted with 20 wt.% of TFVE-biphenol in DMAc or NMP in flask. Low molecular weight of homopolymer was obtained from the appearance of brittle films, which was possibly due to the low reaction temperature (below 200 °C). Later attempts were conducted on glass slides in a heating oven. TFVE-biphenol was dissolved to form a solution and cast on the glass slide before vacuuming the oven and filling nitrogen back in for three times. Casting TFVE-biphenol solution rather then directly put bulk TFVE-biphenol on the glass slide was to avoid any monomer loss during the vacuuming and nitrogen filling process. After the oven was filled with nitrogen, the temperature was increased to 210 °C and the glass slide was left in the oven overnight. Clear and flexible film was obtained after overnight polymerization (Figure 22).

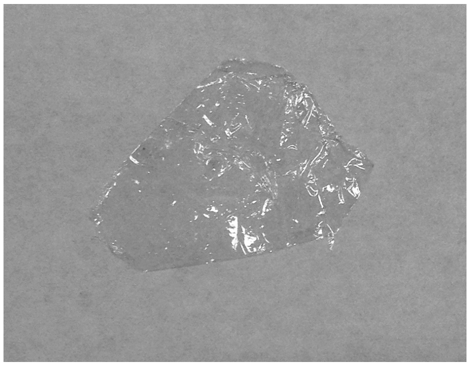

Figure 22. Film of TFVE-biphenol polymer.

6. Processing of silicotungstic acid functionalized fluoroelastomer synthesized using potassium carbonate

6.1 Introduction

Electrochemical energy conversion devices have great potential to replace the internal combustion engine and transform the electrical grid; this can be accomplished with batteries, fuel cells and flow batteries. One main advantage that fuel cells have over batteries when it comes to the automotive sector is the rapid rate of refueling hydrogen is similar to petroleum refueling. While the field has greatly progressed in the last decade, some room for improvement still exists.

From a systems prospective, high temperature operation would be beneficial for water and heat management.[7] Additionally, durability is important in conditions of chemical and mechanical strain that will be experienced in a working fuel cell. One method to solve these challenges is to develop a new membrane that is conductive, strong, and chemically and mechanically durable. Silicotungstic acid is able to conduct at high temperatures with minimal hydration, making it an ideal acidic moiety. [8,9]

This study discusses the synthesis of a new material, followed by investigation if the materials fuel cell performance and mechanical durability. The use of silicotungstic acid (HSiW) results in a film with a low area specific resistance (ASR) at elevated temperatures. A membrane with low ASR has been made through the synthesis of this new material. It is likely that a metastable state of the membrane resulted in these outstanding transport properties and small angle x-ray scattering (SAXS) data suggests that a morphology with features of *ca.* 6.5 and 1.0 nm will occur whenever the membrane is processed under a variety of conditions.

6.2 Materials and methods

Synthesis: First, diethyl (4-hydroxyphenyl) phosphonate (DHPP) is produced using a method previously reported in literature.[10] Next, 20g FC-2145, a commercial poly(vinylidene fluoride-co-hexafluoropropylene), is added to 150 mL tetrahydrofuran (THF), and allowed to dissolve at reflux. Once dissolved, 20g DHPP (1 eq.) is added followed by 30g K_2CO_3 (2.5 eq.) and the reaction solution is allowed to react for 5 days at reflux. Water is added to the reaction to precipitate the polymer at the end of the reaction. The precipitated polymer is then washed with boiling water to remove KF, $KHCO_3$, and unreacted DHPP. Once the KF is washed out, concentrated HCl is added for the hydrolysis of the phosphonate ester. The polymer is then washed with water and stored. The PolyPPA (product of step 3 in Figure 23) is then used for the attachment of Silicotungstic acid (HSiW). The PolyPPA is added to a round bottom flask with n,n Dimethylacetamide (DMAc) and allowed to dissolve. Once the solution is homogenous, the potassium lacuanry HSiW ($K_8SiW_{11}O_{39}$) is slowly added. To start the reaction, 12 M HCl is added (5 mol HCl:1 mol HSiW) and allowed to react for 3 h at 80 °C. The solution is then kept at 4 °C until it is to be used.

Film Forming: The polymer solution is cast on Teflon® at room temperature and allowed to dry overnight in a fume hood. For area specific measurements, the solution was cast on Kapton and removed *via* immersion in water. For the films analyzed with SAXS, the processing conditions are discussed in the text.

MEA fabrication: Gas diffusion electrodes (GDEs) containing 0.5 mg/cm² Platinum on Vulcan (60% Pt) on carbon cloth were purchased from the Fuel Cell Store and were cut to size. The GDEs were then sprayed with several layers of polymer reaction solution, allowing the layer to dry before adding a second layer. Two such GDEs were placed together to form a fuel cell resulting in a membrane thickness of *ca.* 5-15 μm. A second membrane was fabricated with a thicker, freestanding film for the mechanical stress test.

Conductivity and ASR measurements: Electrochemical impedance spectroscopy was used to measure the membrane resistance in-plane and calculate the corresponding material conductivity. The resistance in the through plane direction, assuming isotropic transport properties, was then calculated with the conductivity and thickness. This measurement was done in a Test Equity environmental chamber at the conditions specified within the text.

Fuel cell testing: Two 5 cm^2 fuel cells were tested using Scribner test stands. The testing conditions are described within the text.

Small angle x-ray scattering: SAXS data was collected at the Advanced Photon Source at Argonne National Lab using beamline 12-ID-C with an energy of 18 keV in a custom environmental chamber, as fully described in a previous publication.[11]

6.3 Results and discussion

To the polymer solution, the DHPP and K_2CO_3 were added, resulting in a color change of the solution from clear to dark brown. The color change occurred over several hours until the solution was too dark for additional changes to be noticeable by eyesight. After 5 days, the solution was precipitated through addition of water, followed by reflux in concentrated acid. This resulted in the phosphonic acid form of this polymer (PolyPPA), as seen in the synthetic pathway below (Figure 23, step 3 product).

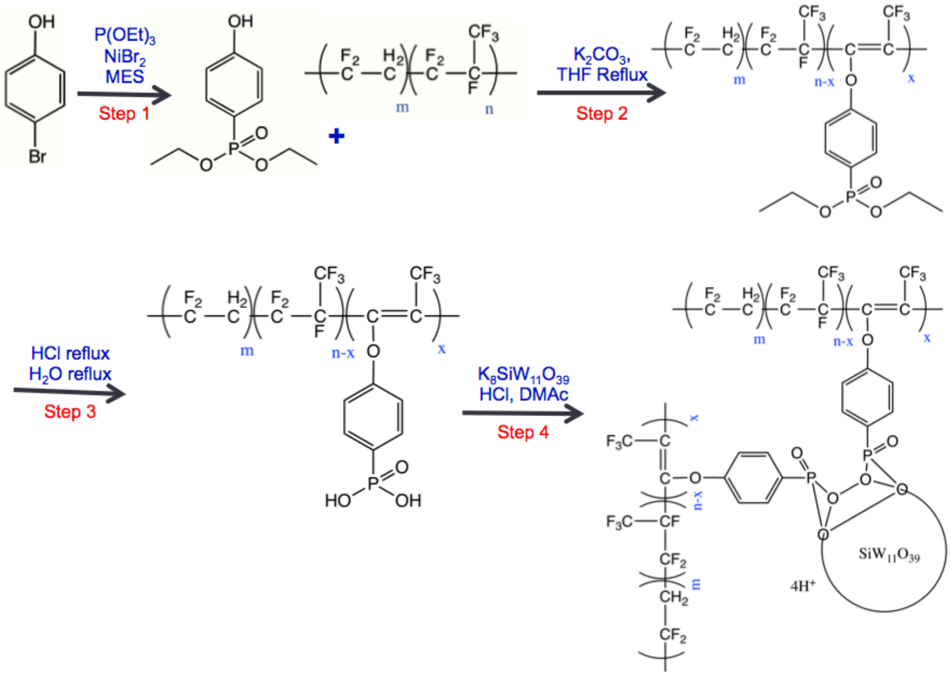

Figure 23: Synthetic pathway for making the PolyHPA material (final product) through a 4 step process. Step 2 and 3 are done in one pot.

The PolyPPA was then isolated, washed, and dried. The dried polymer was then dissolved in deuterated dimethyl sulfoxide (DMSO-d6) for NMR (Figure 24). The initial small molecule has an intense, sharp signal near 21 ppm in ^{31}P NMR. Once this molecule is attached to the polymer and converted to the acid from the ether, the signal seen in ^{31}P NMR is shifted to 12 ppm and becomes broad. The shift is indicative of conversion of the phenol phosphonic ester to the phenol phosphonic acid while broadening is an indication the phosphorous atom is covalent tethered to the polymeric backbone. It is also important to note here that the rest of the spectrum for the polymer has no additional signals, indicating that only one type of phosphorus containing side chain exists in an observable amount.

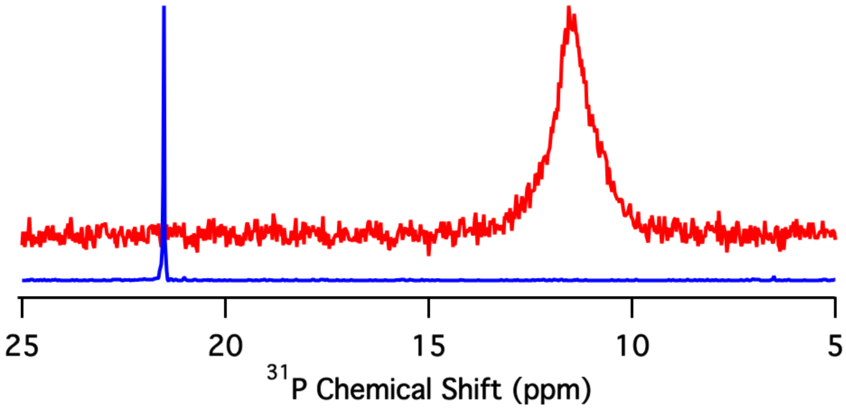

Figure 24: ^{31}P NMR of the reactant and product

The last step to make this material is attaching the HPA. The functionalization of lacunary heteropoly acids with small molecules phenol phosphonic acids has been reported in the literature,[12,13] but this is the first reporting of covalently attaching heteropoly acids directly to a functionalized polymer. For this process, the PolyPPA is dissolved in DMAc at 80 °C. Next the HPA is added, creating a cloudy, viscous mixture. The last step is adding 4 mol H+ per HPA in a dropwise fashion. This results in a clear reaction solution. At this point, the HPA loading is adjusted based on the desired properties of the material. More HPA will result in a more conductive, but more brittle film. Optimization of this process is needed, but the initial results show low ASR is achievable with high levels of HPA loading.

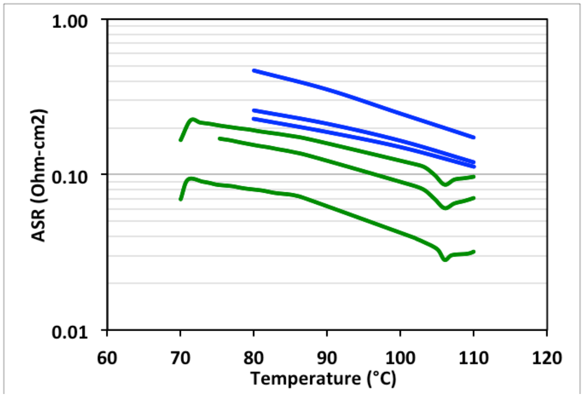

Figure 25: ASR of the material at 50%RH. Blue films are 70 wt% HPA and the green lines represent different trials of a film with 80 wt% HPA loading.

The conductivity of this material was outstanding, but the data was not consistent.

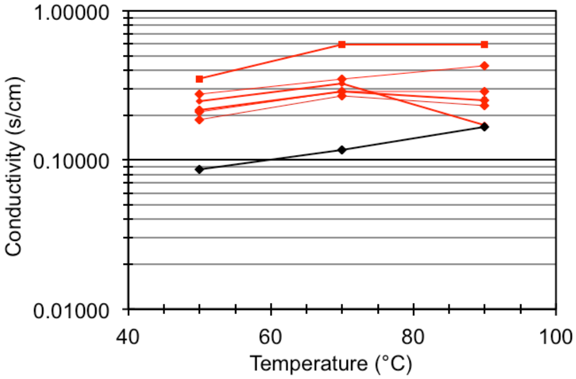

Figure 26: Proton conductivity at 95 %RH for several different films. Processing conditions had no correlation with conductivity.

The films in Figure 26 we all processed differently (drying temperature, annealing process, ion-exchange, and washing). No statistical correlation existed with any of the processing steps. Next, the morphology was investigated.

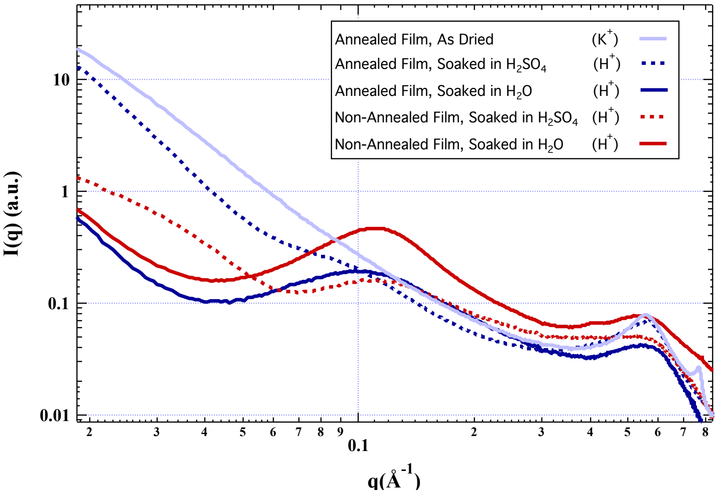

Figure 27: SAXS data through out the film processing from the as-dried film to an ion-exchanged film.

Two peaks appear, indicative of *ca*. 6.5 and 1.0 nm features. First, when the film is dried, only the 1.0 nm feature is present. This feature is attributed to the d-spacing between adjacent HSiW moieties. Next, the film was soaked in acid, resulting in the formation of a shoulder at *ca*. 6.5 nm. This shoulder turns into a peak when the film is soaked in water. When the film is not annealed, the signal at 6.5 nm is more intense. It is then proposed that annealing the films serves to mitigate the formation of this feature. Two opportunities exist to anneal the film: (i) before the film is soaked in acid for the ion-exchange (ii) after the film is soaked in acid and before the film is washed with water. The feature does not appear until the film is soaked in a liquid and in-situ annealing experiments did not show any changes. After the film was soaked in acid, an in-situ annealing experiment resulted in an interesting change, see Figure 28.

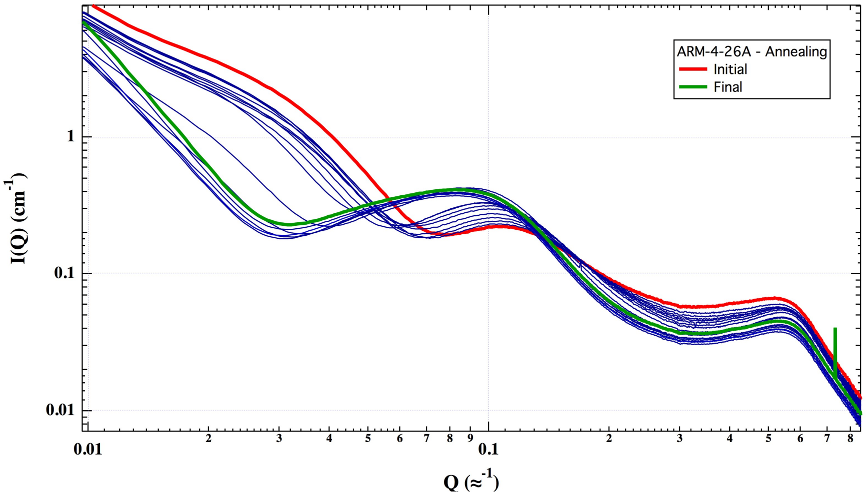

Figure 28: *in-situ* SAXS annealing experiment where the film was heated to 160 °C and held for 15 min then cooled. Transient data was collected every 2 min.

The shoulder is converted into a peak, indicating that annealing after ion-exchange and before washing is not able to fully mitigate the morphology change.

To further probe this, different drying temperatures and annealing after ion-exchange were tested

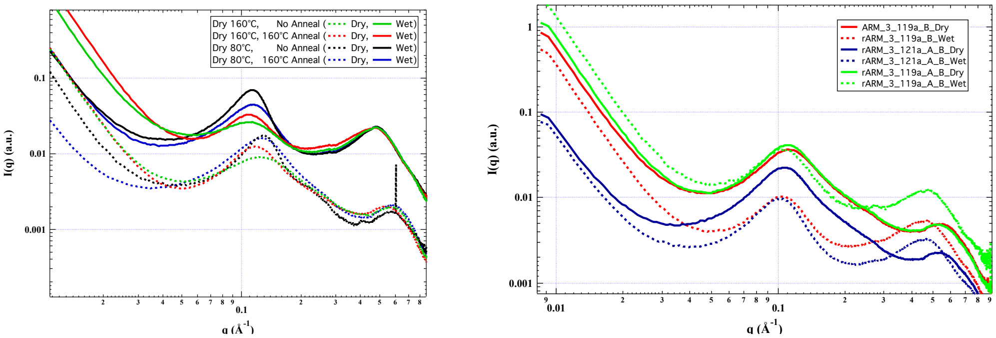

Figure 29: SAXS data for a processing study (left) films that were processed in different ways.

The film drying temperature and annealing process give some change in the intensity and the shape of the peaks, but they persist in all films. These features are also present after boiling.

In conclusion, this peak is always present with this chemistry and under many processing conditions. It is likely a thermodynamically favored state and avoiding it will pose a challenge for this specific chemistry. It is hypothesized that the films that exhibited outstanding conductivity (Figure 26) were in a metastable state, as they were not equilibrated in water for *ca.* 10 min, unlike the days that the samples for SAXS were given. It is proposed that the best opportunity for controlling morphology comes before the ion-exchange step.

Next, to test this material in a device, a fuel cell was fabricated. Direct membrane deposition was used for fabrication because of the benefits reported in literature[14] and the poor mechanics of this film. The directly deposited film had a low cell resistance, resulting in high power density. This fuel cell was using traditional perfluorinated sulfonic acid (PFSA) ionomer in the electrodes, likely leading to part of the performance drop, but high power was achieved at 60°C/75%RH with H_2/O_2 feed and no back pressure. The OCV was 0.914 V and better fabrication is needed to improve this value.

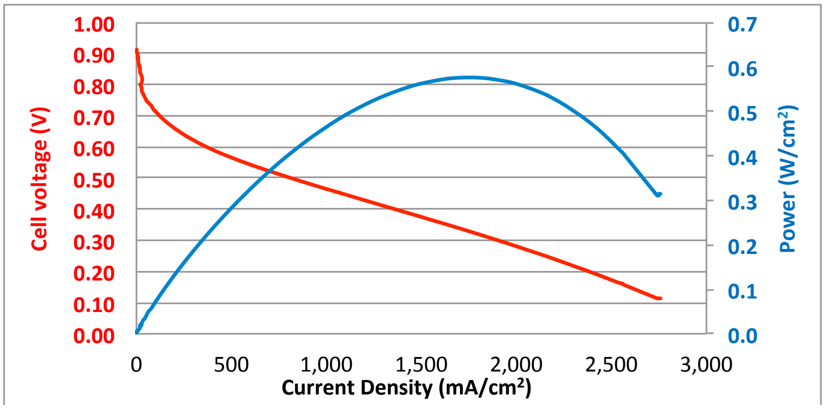

Figure 30: Polarization curve of membrane made with direct deposition method. The cell temperature was 60°C and the inlet humidity was 75%.

As mentioned earlier, the mechanics of this highly cross-linked film are poor, but the crosslinked nature of this material also results in low swelling. It is important to note that an annealing step in excess of 120°C is needed to reduce the swelling. Similar swelling to PFSA has been reported from un annealed films.[15]

6.4 Conclusion

The details of a new synthetic route are discussed that result in a material with low ASR. The key to achieving this low ASR is synthesizing a polymer with only phenol phosphonic acid side-chains, requiring high conversion efficiency. This has been accomplished through attaching a phosphonic ester and subsequent hydrolysis with concentrated HCl. ^{31}P NMR showed high conversion efficiency. Next, the HPA loading was increased, resulting in decreasing ASR. The morphology was investigated with SAXS and this material had two characteristic features, one at 1.0 nm was always present and another feature with a d-spacing value of *ca*. 6.5 nm was present only after soaking in acid and became more pronounced when it was soaked in water. A fuel cells was fabricated using a direct membrane deposition technique and was used for testing the performance at low temperature and low humidity conditions. A power density of 0.6 W/cm^2 was achieved at 60°C and 75%RH and it is proposed that the PFSA ionomer was a limitation for the performance.

7. Optimization of silicotungstic acid functionalized fluoroelastomer synthesized using NaH

7.1 Introduction

Fuel cells are electrochemical energy conversion devices, which can directly convert the energy stored in chemical bonds into electricity. The volumetric and gravimetric power and energy density of polymer electrolyte fuel cells are such that they represent a promising replacement to the internal combustion engine for automotive applications. Major improvements in fuel cell design have been made to simplify the overall system through adoption of thinner membranes, which allow for back diffusion of water and improved performance with dry inlet gasses [[16], [14]]. Additional work to reduce catalyst loading has been successful, resulting in the projected stack cost dropping below $15 per kW when mass produced.[17] These advances have enabled the beginning of commercialization of fuel cell electric vehicles (FCEV). Improved platinum utilization and increased power density would reduce fuel cell stack size and materials cost, further reducing the barriers to fuel cell technology. In addition to reducing the initial cost, durability should be improved. Polymer electrolyte membranes undergo two main types of degradation, chemical and mechanical, and the two degradation pathways have been proposed to have a synergistic effect on each other.[18], [19], [20], [21] For longevity in real world devices, it is thus imperative to have both outstanding chemical and mechanical durability. Adding mechanical support to the membrane is able to satisfy the need for mechanical durability through decreasing swelling and improving strength, but chemical degradation mitigation techniques are still not satisfactory for the needs of a fuel cell system.[22], [23]

Polymer electrolyte membranes need to have good ion-transport, high electrical resistance, and provide a good barrier to reactant gasses for good performance and also need to be durable under conditions in which a real device will experience. Many new materials have been synthesized and studied, but none have been able to simultaneously meet all of the aforementioned criteria and provide enough benefit over the perfluoro sulfonic acids (PFSAs) for wide adoption.[24], [25], [26], [27] One potential factor is the reliance on the pendent sulfonic acid groups in a majority of these materials which require high water content, high concentration of protons, or both to result in ionic conductivity over 0.1 S cm-1. One notable advance in hydrocarbon membranes is the use of a coating containing nanocracks, which are able to act at a barrier to loss of water at elevated temperatures, and thus retain high proton conductivity under low humidity conditions.[28] A large number of these materials are hydrocarbon based and chemical stability data is not available.

Preliminary efforts to improve the chemical stability of the PFSA polymers was to treat the polymer with elemental fluorine to minimize the number of reactive carboxylic acid end groups, but once main chain scission occurs this method becomes ineffective.[29], [30] Second generation efforts to improve the chemical stability of the PFSA materials was to add some radical decomposition catalyst, most notably CeO2 or MnO2.[31], [32], [23] These additives can be introduced as a composite material or the Ce3+ and Mn2+ ions can partially neutralize the H+ ions, effectively lowering the number of protons available for transport and therein reducing the cell performance. There is a trade-off where durability is greatly improved, but the performance is not greatly decreased, unfortunately, the Ce3+ and Mn2+ ions are still free to move in the electrolyte domain and accumulation of them in the cathode catalyst layer is cause for concern.[33], [34], [35] More recently a composite approach has been demonstrated using zirconia doped ceria additives which show further reduction of open circuit voltage loss.[36]

An alternative class of additives that have shown promise in mitigating chemical degradation are heteropoly acids (HPAs), a sub-class of the polyoxometalates. [9], [37], [38], [39] HPAs are a large class of super acids, which also may serve as radical decomposition catalysts. It is important to note here that phosphotungstic acid (H3PW12O40) will decompose in the presence of radicals forming the Ishii-Venturello catalyst, whereas silicotungstic acid (H4SiW12O40) is known to be stable under similar conditions.[40], [41], [42] Phosphotungstic acid and its caesium salt have shown the ability to improve both the proton transport and chemical stability of sulfonated poly-(ether ether ketone) (sPEEK), but using this approach has not yet been proven to result in performance and stability parity with N211.[43], [44] Past efforts to incorporate HPAs into membranes have been hindered due to the HPA migration, clustering, or leaching out due to their high solubility in water.[45], [46] One potential solution to this challenge that has recently been investigates is encaposlating the HPA in carbon nanotubes.[47], [48] In addition to the antioxidant properties of HPAs, they are also known to be very conductive even with limited hydration.[49], [50] By acting as an ion conducting moiety and a radical scavenger, a win-win situation occurs where more HPA can theoretically increase the H+ transport and increase the chemical stability, bypassing the trade-offs associated with Ce and Mn doping. More recently our group has demonstrated a material with covalently immobilized HSiW as the only ion-conducting group, resulting in a shift in the paradigm from previous HPA containing membranes. [51], [8]

Herein, we report a three-step, highly efficient synthesis producing a membrane achieving the chemical durability breakthrough the community has been searching for. Using a novel ion-conducting material that contains HSiW hybrid moieties covalently bound to a commercial fluoroelastomer, resulted in a thin, conductive, and chemically robust membrane. We have demonstrated that this material has lower, in-situ transport resistance and vastly greater chemical stability than the state of the art polymer electrolyte.

7.2 Experimental

Materials: Diethyl (4-hydroxyphenyl)phosphonate (DHPP) was purchased from Synquest (catalog number 6677-1-07) and a polyvinylidene-co-hexafluoropropylene (PVDF-HFP) fluoroelastomer (FC-2178) was supplied by 3M. Hydrochloric acid (HCl) (37%, ACS reagent grade) was purchased from Pharmco-Aaper. Sodium hydride (NaH) (60% dispersion in oil) and bromotrimethylsilane (TMSBr) (97%) were purchased from Sigma-Aldrich. All other reagents were purchased from Sigma-Aldrich with >99% purity and were used as received.

Preparation of PolyPPE: FC-2178 (31.78 g) was washed with methanol, dried at 40°C under vacuum for two days, then dissolved in 150 mL anhydrous dimethylformamide (DMF). In a separate flask, 20.0 g DHPP was added to 100 mL anhydrous DMF and allowed to dissolve at room temperature, followed by cooling to 0°C. Once cooled, NaH was added slowly to the DHPP solution, under a $N_{2(g)}$ flow, producing $H_{2(g)}$ bubbles. After 2 h, bubble formation subsided and the FC-2178 solution was slowly added over a period of 30 minutes. The combined solution was then heated to 50°C and allowed to react for 24 h, darkening with time, before precipitation in 1M HCl. The precipitate is then isolated, washed with water, and dried under vacuum for 48 h, producing phenol phosphonic ester functionalized FC-2178 (PolyPPE).

Preparation of PolyPPA: The PolyPPE was then dissolved in 450 mL acetonitrile overnight at room temperature. The following day, 32 mL bromotrimethylsilane (TMSBr) was added under a N_2 environment. The reaction was heated to 45°C and allowed to react overnight, producing a cloudy mixture. The reaction solution was filtered and the filtrate was dissolved in 600 mL MeOH with 20 mL concentrated HCl, quenching the reaction. The reaction solution was dried resulting in the phenol phosphonic acid functionalized FC-2178 (PolyPPA). The PolyPPA was subsequently washed with water, dried, and stored at room temperature, yield = 38.5g (77%).

Preparation of PolyHPA: 4.50 g PolyPPA was added to 180 mL *n*,*n*- dimethylacetamide (DMAc) and allowed to dissolve overnight at 80°C. Next, 10.50 g α-$K_8SiW_{11}O_{39}$•13(H_2O) (HSiW), synthesized according to the protocol previously reported,[40] was slowly added. The mixture was cloudy, but rapid stirring with a magnetic stir bar ensured no precipitate formed on the bottom. Next, 12 M HCl (1.356 mL) was added dropwise, turning the solution into a transparent amber. The reaction took place over 70 h at 80 °C, then the solution was filtered with a paper filter followed by a filtration using a medium porosity glass frit Büchner Funnel to remove potassium chloride crystals. The volume was then reduced to ca. 60 mL using a rotary evaporator. This solution was then cast on Kapton® using a doctor blade to control thickness and dried at room temperature over night (16 h). When dried, the films ranged from 20-80 μm. Next, thermal annealing under pressure (5 min, 26.7 kN, 160°C) was used to finish the attachment reaction and make the film more uniform. The resulting film was then soaked in 1 M H_2SO_4 to ion-exchange (3x) followed by rinsing in DI water (3x). Each rinse was more than 1 h.

Materials Characterization: Fourier Transform Infrared Spectroscopy (FT-IR). FT-IR was collected using a Nicolet Nexus 470 FT-IR E.S.P equipped with a Specac Golden Gate attenuated total reflection (ATR) stage at ambient conditions. All spectra were collected with 512 scans and a resolution of 1 cm^{-1}. All polymers were measured in the membrane form and the small molecules were measured as powders.

Nuclear Magnetic Resonance Spectroscopy (NMR). Liquid NMR spectra were recorded on a Joel ECA 500 MHz spectrometer in DMSO-d6 solvent. The chemical shifts for ^1H, ^{19}F, ^{31}P were based on tetramethylsilane, trichlorofluoromethane, and phosphoric acid standards, respectively. The solid state $^1H \rightarrow {}^{31}P$ CP/MAS measurements were performed on a 400 MHz Bruker spectrometer using triphenylphosphine (-6ppm) as a standard.

Thermogravimetric Analysis (TGA). TGA experiments were performed using a TA instruments TGA Q 500 using a platinum pan. The ramp rate was 5 °C per minute up to 800 °C with a gas flow rate of 40 mL min^{-1}. Samples were dried at 80 °C for 1 hr followed by equilibration at ambient conditions for an additional hour. Experiments were run using N_2 or air.

Differential Scanning Calorimetry (DSC). The DSC data was collected on a TA instruments DCS Q20 in TZero aluminum pans with hermetic lids. The heating scan rate was 10 °C min^{-1} and the cooling rate was 40 °C min^{-1}. Two cycles from -30 to 130 °C were first conducted, followed by two cycles up to 200 °C.

Potentiostatic Electrochemical Impedance Spectroscopy (PEIS). PEIS experiments were performed in a TestEquity environmental chamber to accurately control the temperature and relative humidity. The membranes were placed across four platinum electrodes in cells designed after Bekktek FC-BT-115 conductivity cells and the PEIS measurements were performed using a BioLogic VMP3 potentiostat. Data were fit using a Randles circuit and the results were used to calculate an in-plane conductivity.

Focused Ion-Beam (FIB) milling and Transmission Electron Microscopy (TEM). The sample was milled with Gallium ions using a Helios NanoLab 600i focused ion beam and placed on a TEM grid. The transmission electron microscopy (TEM) was performed using a FEI TalosF200X.

Small Angle X-ray Scattering (SAXS). The SAXS data was collected on beamline 12-ID-B at the Advanced Photon Source, Argonne National Lab in a custom built environmental chamber, using 13.3 keV radiation. The chamber, described in detail elsewhere,[52] is able to control temperature and humidity and the conditions are outlined below. A Pilatus 3M detector was used.

Environmental Scanning Electron Microscopy (ESEM) and Energy Dispersive Spectroscopy (EDS). The electron scanning microscope used was a FEI Quanta 600 operating under low vacuum. All SEM images shown were taken with a solid-state backscatter electron detector. The EDS was performed with an element EDAx at 20 keV. Standard parameters were used to quantify elements using EDAx Genesis software.

Fuel Cell Testing: The Nafion® standard membrane electrode assembly (MEA) was fabricated using a catalyst coated membrane (CCM), N211, with catalyst supplied by Tanaka Holdings Co. Ltd. The anode catalyst layer consisted of TEC10EA30E, 30% Pt/C, 0.055 mg cm^{-2} and a cathode catalyst layer consisted of TEC10E50EHT, 50% Pt/C, 0.35 mg cm^{-2} and had an active area of 2x5 cm^2. The PolyHPA MEAs were fabricated using commercial gas diffusion electrodes (GDE)s for both the anode and cathode (((Johnson Matthey Pt/C electrocatalyst, PFSA ionomer, 0.35 Pt mg cm^{-2}). The PolyHPA-70 (70 wt% theoretical HSiW loading) MEA had an active area of 2x5 cm^2 and the PolyHPA-75 (75 wt% theoretical HSiW loading) MEA was 5 cm^2. The 10 cm2 fuel cells were run using flow rates, 4 L min^{-1} at the anode and 8 L min^{-1} at the cathode while the 5 cm^2 fuel cell was run using flow rates of 2 L min^{-1} at the anode and 4 L min^{-1} at the cathode.

Accelerated Stress Testing (AST): The mechanical AST was performed on an MEA in standard fuel cell hardware at 80 °C with N_2 flow on both the anode and cathode and the humidity of each was switched from 100 %RH to 0 %RH holding for 30s on each, making a 1 min cycle. The test was stopped and hydrogen crossover was tested using linear sweep voltammetry with a scan rate of 1 mV s-1, after 5750, 10000 and 22500 cycles. The chemical ASTs were performed on an MEA in standard fuel cell hardware by holding the fuel cell at open circuit voltage (OCV), 90°C, 30%RH anode and cathode, zero current, and H_2/O_2 flow.

7.3 Results and Discussion

Synthesis: A four-step synthesis, reported elsewhere,[53] was used to covalently attach HSiW to FC-2178, where hexafluoropropylene accounts for ca. 20 mol% of the polymer.[54] This original synthesis method involved attachment of diethyl (4-hydroxyphenyl)phosphonate (DHPP) sidechains to FC-2178 utilizing K_2CO_3 as a reactant. The K_2CO_3 can ion-exchange with the alcohol to form an alkoxide ($-O^-K^+$) and potassium bicarbonate ($KHCO_3$). Both alkoxide and K_2CO_3 are then able to dehydrofluorinate the FC-2178, creating unsaturated bonds, and enabling attachment of the alkoxide. Because K_2CO_3 is a poor nucleophile, it will not attach to the polymer and only the alkoxide will become covalently attached. This chemistry is based on methods that have been used to cross-link PVDF-HFP.[55], [56] The reaction resulted in excessive unsaturated bonds remaining in the final product and the films had extremely poor mechanical properties.

To avoid the over dehydrofluorination, the reagent was changed to NaH, as the hydride is a stronger base than K_2CO_3, but still a weak nucleophile. This change allows for attachment of DHPP at much lower temperatures. The resulting phenol phosphonic acid functionalized FC-2178 (PolyPPA, see Scheme 1), a transparent yellow film, was much lighter in color than the PolyPPA made using K_2CO_3, which was almost black. The work described here was done using the much stronger PolyPPA produced via. the process outlined in Scheme 1.

The method for functionalizing lacunary heteropoly acids with small organic molecules has been well documented,[13], [12] but this work involves attaching HSiW to a preformed engineering polymer chosen for its strength and stability.

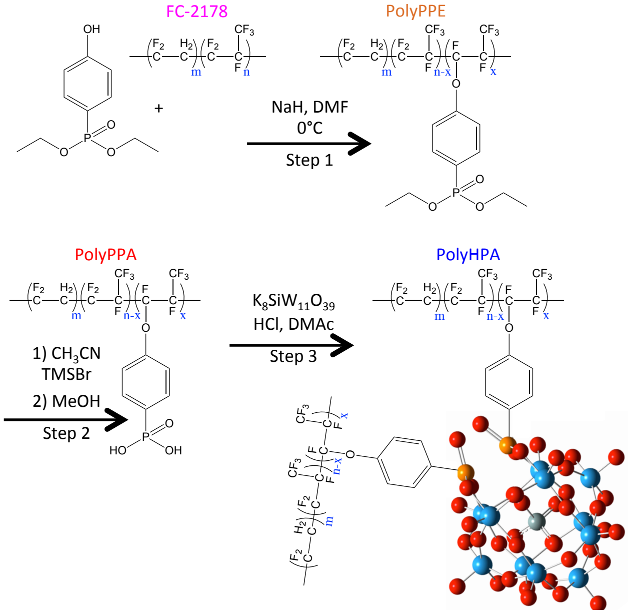

Scheme 1: Full synthetic reaction scheme for the synthesis of PolyHPA (final product) from FC-2178 and DHPP

Attachment of HSiW to a preformed polymer, to the authors knowledge, has not been previously reported in the peer-reviewed literature.

The final product is referred to as PolyHPA-x where x indicates the mass fraction of α-$K_8SiW_{11}O_{39}$•13(H_2O), added to the reaction (Scheme 1, step 3), with the remaining mass consisting of PolyPPA. A majority of the studies were done on PolyHPA-70 and some data exist for the higher loading material, PolyHPA-75. Unfortunately at 75 wt% loading the mechanics of the film resulted in challenges for more comprehensive fuel cell testing, but what was achieved, see below, shows much potential for the future use of these films. For the fuel cell testing of the PolyHPA-75 material, a 10 cm^2 MEA could not be fabricated and the active area was 5 cm^2. All films were thoroughly washed in acid followed by water at room temperature showing that the HSiW moiety was indeed covalently attached. IR and NMR characterization and discussion is available in the supplementary information (SI).

IR spectra for species involved in the functionalization of FC-2178 to form PolyPPA can be seen in Figure 31: a. The IR spectra are dominated by the -CF_2- stretching bands at 1200 and 1130 cm-1 (symmetric and asymmetric, respectively) for FC-2178 and the PolyPPA.[57] Strong bands from the aromatic group at 1200 and 1180 cm^{-1} are present in both the DHPP and the PolyPPA, as expected. While the C-O-Ar bond formed in step 1 is not identified, the washed functionalized PolyPPA shows signatures of aromatic groups, which would have washed away if not covalently attached to the polymer. The next step in the synthesis is attaching HSiW to the PolyPPA. The reactants and product for the attachment of HSiW to PolyPPA are displayed in Figure 31: b. It is evident that signatures from both HSiW and PolyPPA exist in the washed PolyHPA. Most notably are the -CF_2- stretching bands and the strong W-O bands between 700 and 1000 cm^{-1}.[58]

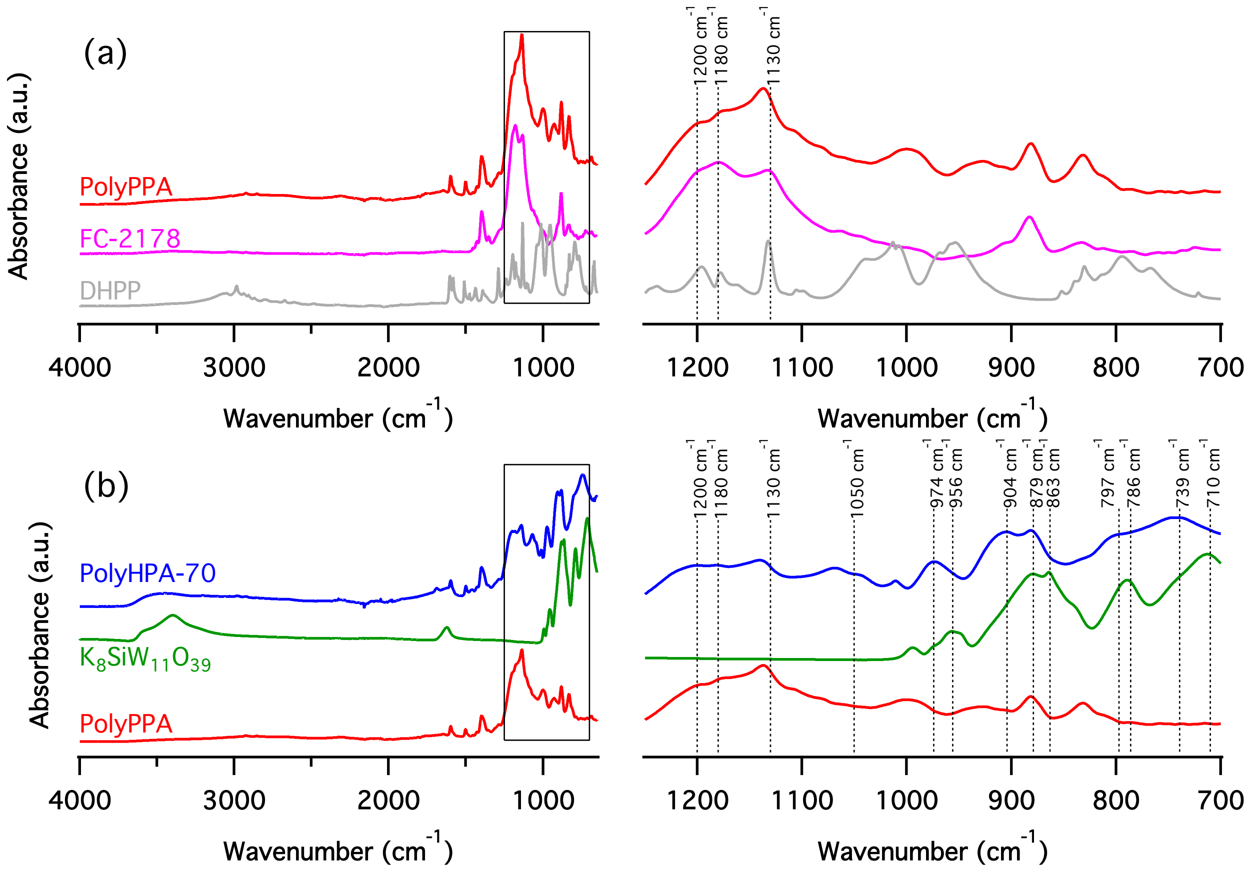

Figure 31: (a) IR data of the reactants and products for the attachment of phenol phosphonic acid side chains to FC-2178 (step 1 and 2 in scheme 1) with an expanded view of the boxed area displayed to the right (b) IR data of the reactants and product for the HSiW attachment to PolyPPA with an expanded view of the boxed area displayed to the left.

More thorough analysis of these bands indicates a shift to higher wavenumbers after the attachment, as expected from the aforementioned work with attaching small, organic molecules. Additionally, a peak at 1050 cm^{-1} is present in the product and neither of the reactants. Previous studies have concluded that in phenylphosphonic acid ν_{as}(P-OH) is located at 1017 cm^{-1} and for $[\gamma\text{-SiW}_{10}\text{O}_{36}(\text{C}_4\text{H}_5\text{PO})_2]^{4-}$ ν_{as}(P-OW) is located at 1050 cm^{-1}.[59, 13] A list of assignments are presented in Table 1. While the IR data provides compelling evidence that the synthesis has occurred as expected, NMR was used to corroborate the covalent attachment of HSiW.

Table 1: Assignments of FTIR bands in cm-1 according to previous studies [13], [12], [58]

	K8SiW11O	PolyHPA
ν_{as}(P-O)	-	1050
ν_{as}(Si-Oa)	956	974
ν_{as}(W=Oter)	879	904
	863	879
ν_{as}(W-Oe-	768	797
ν_{as}(W-Oc-	710	739

Further evidence for the validity of the synthetic scheme was provided by ^{1}H NMR (Figure 32: a). First in the DHPP, the aromatic protons are located at 6.9 and 7.5 ppm and the $-CH_2-$ and $-CH_3$ chemical shifts are at 3.9 and 1.2 ppm, respectively. The $-CH_2-$ groups in the FC-2178 are located between 2.7 and 3.3 ppm. When the DHPP is attached to the polymer, the product contains the same $-CH_2-$ signals from the FC-2178 in addition to the aromatic signals and the signals at 3.9 and 1.2 ppm. Next, the hydrolysis reaction is performed on the PolyPPE and the phosphonate ester $-CH_2-$ and $-CH_3$ chemical signatures are eliminated, as expected, and a new signal exists at 6.5 ppm and is assigned to the -OH bonds.
The ^{19}F NMR (Figure 32: b) indicates that when adding the sidechain, an additional signal at -55 ppm appears which is consistent with other studies on PVDF-HFP functionalization.[60] Perhaps the most compelling evidence for the functionalization of the polymer comes from ^{31}P NMR (Figure 32: c and Figure 32: d). First, when the DHPP is attached to the polymer there is a change in chemical shift (21→ 17.5 ppm) and the signal becomes more broad and complex, one indication that the P nuclei are associated with a polymer. At this point, some unattached DHPP is still present (sharp signal at 21 ppm), but after the hydrolysis step, the sharp signal at 21 ppm vanished and the only peak is at 12 ppm (the expected shift for PolyPPA). The final HSiW attached film is cross-linked and not soluble in NMR solvents; therefore, liquid 31P NMR is not possible on the final film. To probe the chemical nature of the final material 31P CP/MAS NMR was performed on both PolyPPA and PolyHPA-70. The chemical shift of PolyPPA is different in the solid phase than it is in the liquid NMR likely due to the water content and solvation and is shown for comparison to the PolyHPA-70 (Figure 32: d). Using a Gaussian fit to model the spectra, four chemical shifts are identified (23, 20.5, 15.1, and 9.5 ppm). The signal at 20.5 ppm is residual phenol phosphonic acid. The three remaining signals are assigned to HSiW with one phosphorous attachment (23 ppm), HSiW with two phosphorous attachments (15.1 ppm), and a phosphorous anhydride (9.5 ppm).[61] The phosphorous anhydride is presumably formed between two unreacted phenol phosphonic acid side chains at elevated temperatures through the loss of a water molecule.

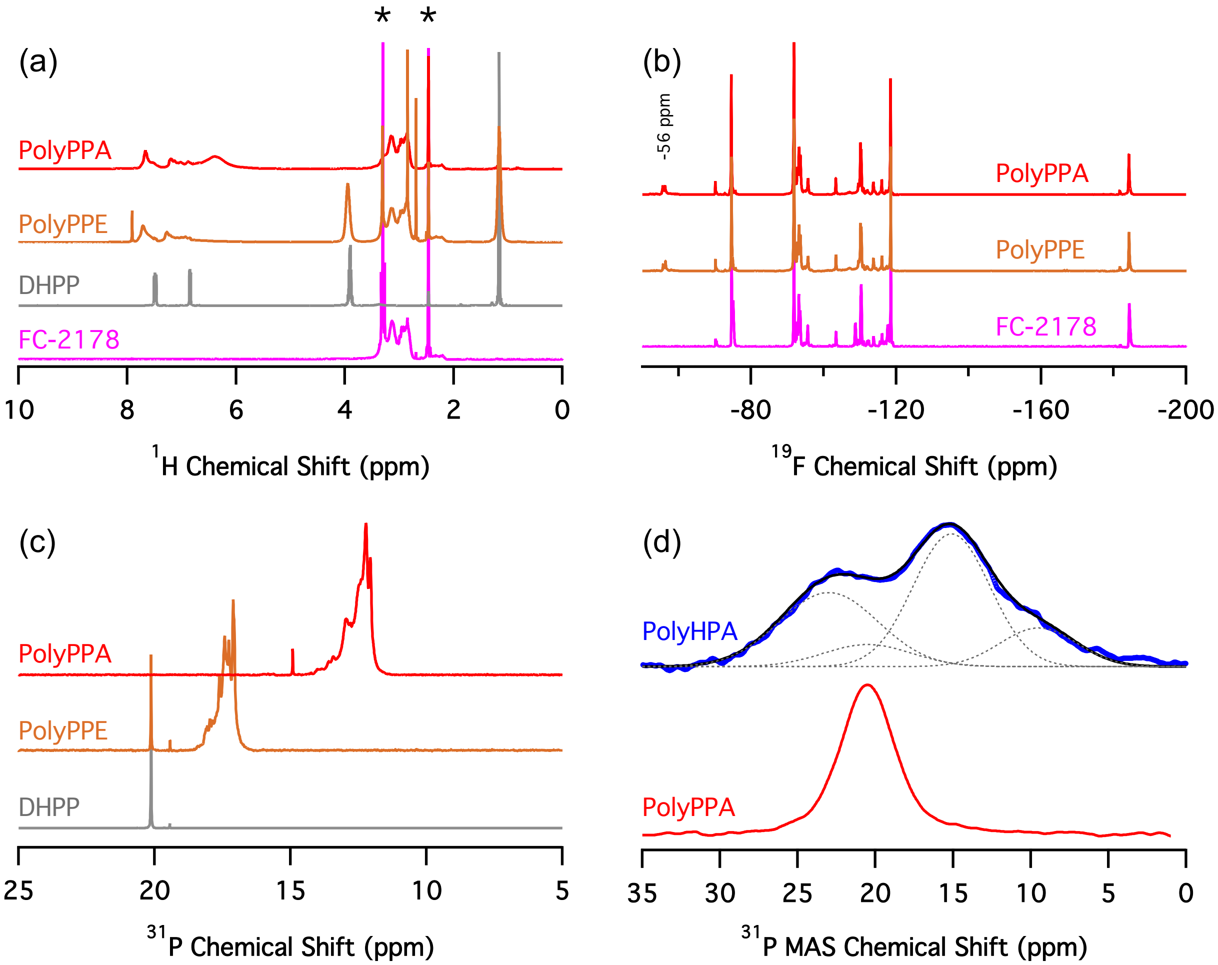

Figure 32: (a) ^{1}H NMR for PolyPPA, PolyPPE, DHPP, and FC-2178 where the remaning solvent signals are labelled * (b) ^{19}F NMR data for PolyPPA, PolyPPE, and FC-2178 (c) ^{31}P NMR of DHPP, PolyPPE, and PolyPPA (d) ^{1}H → ^{31}P CP/MAS NMR of PolyPPA and PolyHPA-70 where the PolyHPA-70 spectra is modelled using 4 different Gaussian functions

<u>Membrane Characterization (Ex-situ Evaluation):</u> The thermal stability was investigated with TGA on the PolyPPA and PolyHPA-70, see data in Figure S3. The PolyPPA has several distinct decomposition regions. First, marginal weight loss occurs before 280 °C, all of which has been assigned to loss of water and has been previously observed in HPA containing materials.[62], [63] Next, between 280 and 400°C there is a constant and substantial loss at 0.2% per °C. Finally, two inflection points exist at 420°C and 490°C where the latter only exists in the presence of air, a more oxidizing environment. PVDF-HFP has a thermal decomposition temperature near 450°C in N_2,[64], [54] but no significant mass loss occurs beforehand. This indicates that the decomposition event starting at 280 °C is likely due to the decomposition or loss of the sidechain.

Due to instability of HPAs at high pH, the IEC was calculated using data from TGA. The TGA data below in Figure 33: , which shows that at 800 °C in air nearly all of the PolyPPA has volatilized < 4 % remaining. Conversely, the PolyHPA-70 has a residual normalized mass of 56 %. This calculation assumes that each silicotungstic acid moiety has 13 hydrating waters at room temperature and humidity, a common hydration state of the monolacunary silicotungstic acid.[65],

[66]. Assuming that in air at 800 °C each elements is in its most oxidized form would result in 11 WO_3 and 1 SiO_2 for each HSiW, which has been previously observed for $\alpha\text{–}H_4SiW_{12}O_{40}$ using x-ray diffraction and FTIR.[63]

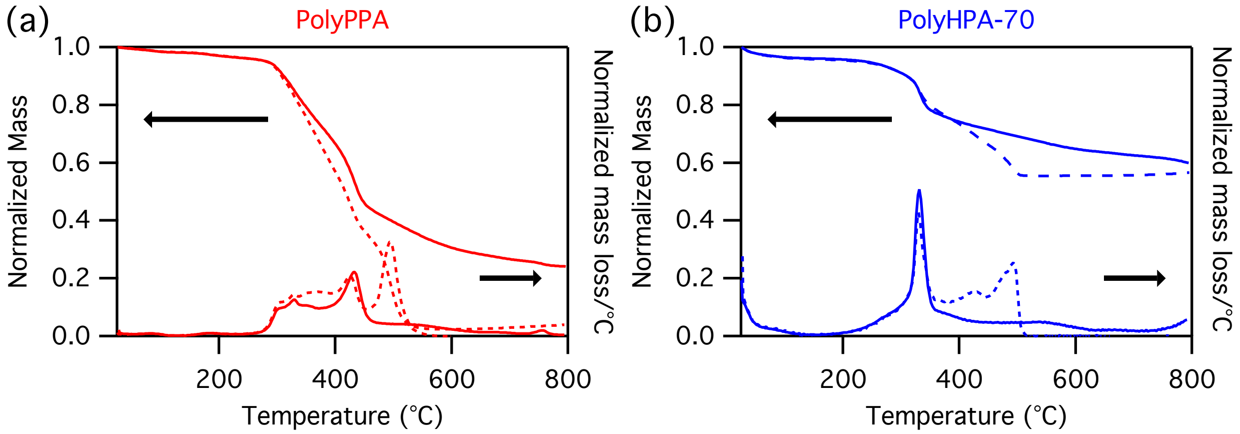

Figure 33: TGA data in N2 (solid lines) and air (dashed lines) for (a) PolyPPA residue in air at 700°C is 2% (b) PolyHPA-70 residue in air at 800°C is 56%.

Calculating the actual IEC from the TGA residue:

$$\left(\frac{1\ mol\ SiW_{11}O_{39}}{11\ mol\ \ WO_3 + 1\ mol\ SiO_2}\right) * \left(\frac{4\ mol\ H^+}{1\ mol\ \ SiW_{11}O_{39}}\right) * \left(\frac{11\ mol\ \ WO_3 + 1\ mol\ SiO_2}{11 * 231.8 + 1 * 60.8\ g\ residue}\right) = \frac{0.0015\ mol\ H^+}{g\ residue}$$

$$\left(\frac{0.56\ g\ residue}{1\ g\ Polymer}\right) * \left(\frac{0.0015\ mol\ H^+}{g\ residue}\right) * \left(\frac{1000\ mmol\ H^+}{1\ mol\ H^+}\right) = \frac{0.86\ mmol\ H^+}{g\ Polymer}$$

Calculating the theoretical residue from adding 70 wt% $\alpha\text{-}K_8SiW_{11}O_{39}\bullet 13(H_2O)$ and 30 wt% PolyPPA:

$$\left(\frac{0.70\ g\ \ K_8SiW_{11}O_{39}\cdot 13H_2O}{1\ g\ PolyHPA}\right) * \left(\frac{1\ mol\ \ K_8SiW_{11}O_{39}\cdot 13H_2O}{3221\ g\ \ K_8SiW_{11}O_{39}\cdot 13H_2O}\right) * \left(\frac{11\ mol\ \ W}{1\ mol\ \ K_8SiW_{11}O_{39}\cdot 13H_2O}\right) = \frac{0.00239\ mol\ W}{g\ PolyHPA}$$

$$\left(\frac{0.00239\ mol\ W}{g\ PolyHPA}\right) * \left(\frac{1\ mol\ WO_3}{1\ mol\ W}\right) * \left(\frac{231.8\ g\ WO_3}{1\ mol\ WO_3}\right) = \frac{0.554\ g\ WO_3}{g\ PolyHPA}$$

If we add 70wt% $\alpha\text{-}K_8SiW_{11}O_{39}\bullet 13(H_2O)$, we would expect to have 55.4% residue at 800°C if all is converted to WO_3 which matches very well with the 56% observed experimentally. The discrepancy may be due to unvolatilized PolyPPA residues.

An additional technique that was attempted to use for determination of the loading of HSiW was EDS, see Figure 34: . First, the SEM figure shows that the PolyHPA-70 membrane is much brighter than the PolyPPA membrane in the backscatter micrograph, one indication that we do have a large amount of heavy elements in the washed film. Additional evidence comes from the W signature in EDS, which is very prominent in the washed PolyHPA-70 film. While quantitative values are given, they are unrealistic and unreliable and should only be considered as semi-quantitative evidence that a large amount of W is present in the film after HSiW attachment and subsequent acid and water washes.

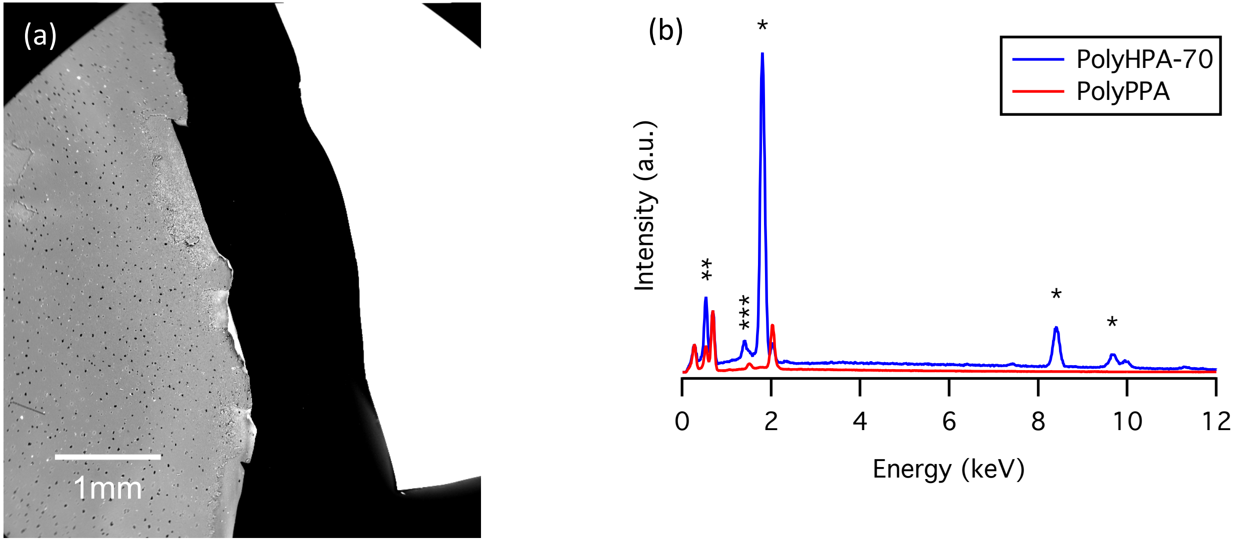

(c)

	PolyPPA		PolyHPA-70	
	wt%	at%	wt%	at%
C	34.7 ± 0.5	46.5 ± 0.7	10.2 ± 1.3	28.7 ± 0.4
O	17.5 ± 0.5	17.6 ± 0.5	13.9 ± 3.0	29.0 ± 2.7
F	33.9 ± 1.0	28.7 ± 0.8	8.7 ± 1.8	15.4 ± 1.4
Al	1.4 ± 0.1	0.8 ± 0.1	0.3 ± 0.1	0.4 ± 0.1
Si	0.2 ± 0.1	0.1 ± 0.1	12.6 ± 0.4	15.2 ± 2.1
P	11.9 ± 0.3	6.2 ± 0.1	1.3 ± 0.0	1.5 ± 0.2
W	0.5 ± 0.2	0.0 ± 0.0	52.9 ± 5.6	9.8 ± 2.0

Figure 34: (a) SEM of PolyPPA (left) and PolyHPA-70 (right) (b) EDS data comparing PolyPPA and PolyHPA-70 to each other where the PolyHPA data was normalized using C Kα and F Kα from PolyPPA. Discrepancies are the result of added W (*) and O (**). The Al peak (***) is also different. (c) Table with calculated values for abundance of the difference elements

HPAs can undergo a loss of two H^+ and a terminal oxygen to form water, thereby reducing the concentration of mobile H^+ in the film. This decomposition is difficult to discern from loss of bound water and theoretically has a strong variance on partial pressure of water.[67] With the high decomposition temperature of this material, it is mostly limited by loss of charge (not seen in TGA). In an oxidizing environment, HSiW moieties are known to decompose into WO_3 and SiO_2, the most oxidized forms of W and Si.[63]

HPAs are known to be unstable in alkaline conditions and therefore traditional titrations to measure ion-exchange capacity (IEC) are not possible and therefore the WO_3 and SiO_2 residue mass was used to calculate the IEC. This calculation, available in the SI, suggests that a large portion of water stable inorganic material has been added to the polymer. The residue at 800 °C in air is ca. 4 % and 55 % for the PolyPPA and PolyHPA-70, respectively. The resulting IEC of 0.86 mmol H+/ g PolyHPA-70 indicates that nearly all of the added HSiW is stable to soaking in acid followed by water at room temperature, for more details, please see the SI. These films are stable to acidic and aqueous environments at room temperature and humidified air at elevated temperatures, but when the films are soaked in warm water (80 °C) some of the HSiW leaches out.

The DSC data can be seen in Figure S4 and has two clear transitions. First, at 60°C there is a thermal transition in both the PolyPPA and PolyHPA-70. The T_α for PVDF-HFP with a similar monomer ratio is -13 °C and so we assign this new transition to the T_β of the sidechains.[68] According to the 31P NMR data, some of the phenol phosphonic acid sidechains still exist in the final PolyHPA-70 film and therefore the T_β is still observed. In the first heating of the PolyHPA-70 (non-annealed) there is an endothermic transition starting near 160°C which could be a chemical reaction or crystallization. An in-situ SAXS annealing experiment was performed on PolyHPA-70 (non-annealed) to observe the morphological changes when annealed, but no indication of change in the morphology was observed, (see Figure 35:).

Using DSC and SAXS, the thermal behavior of the unannealed PolyHPA-70 was investigated, see Figure 35:. Contrasting the DSC data for PolyPPA (Figure 35:a) with the DSC data for PolyHPA-70 (Figure 35:b) one key difference exists; an exothermic event between 120 and 200 °C for the PolyHPA-70. This event was thought to be either an irreversible change in morphology (crystallization) or a chemical reaction. To further probe this event, an in-situ SAXS experiment was performed (Figure 35:c). An unannealed PolyHPA-70 film was loaded in an environmental chamber and dynamic SAXS data was collected as the temperature was ramped up to 160°C and then held for 5 min before cooling to room temperature. The SAXS pattern showed the 6.5 nm clustering the entire time and it is concluded that the exothermic event observed in DSC was not the formation of these clusters or any other morphology change. This exothermic event is therefore assigned to an exothermic reaction. The two potential reactions are additional HSiW attachment to PolyPPA side chains or two PolyPPA side chains reacting with each other to form a phosphorous anhydride. ^{31}P NMR evidence for a change in the P environments between the polymer solution that was cast and the final, annealed film can be seen in Figure 35:d. For fair comparison, the PolyPPA signal has been set to 12.5 ppm as an internal standard to allow comparison between the liquid and solid-state NMR data. The relative abundance of the phenol phosphonic acid signal is lower after the high pressure annealing step, indicative of its involvement in a reaction. This reaction is assigned to result from contributions from both additional HSiW attachment and formation of an anhydride through the loss of water resulting in a new signal more downfield from all of the other ^{31}P chemical shifts.

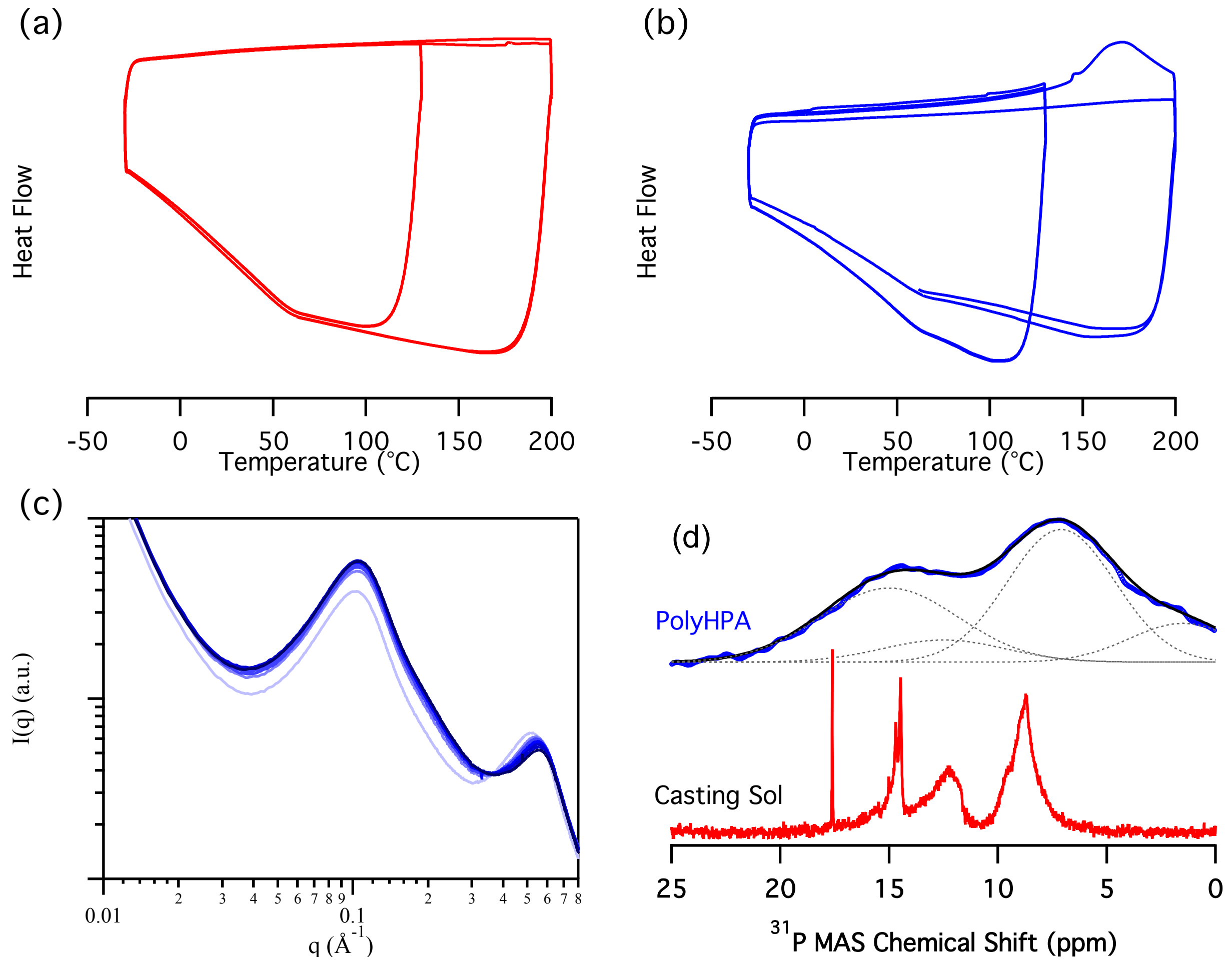

Figure 35: (a) DSC of PolyPPA (b) PolyHPA (c) SAXS data for an in-situ annealing study where the film was heated from room temperature to 160°C then held for 5 minutes. Notice the clustering is present through out the experiment.

Using this knowledge, all films were processed at 160°C for 5 min to enhance crosslinking and avoid thermal decomposition.

The proton conductivity, seen in Figure 36, is >0.1 S cm^{-1} at all of the temperatures measured (50-90 °C and 95 %RH) and exhibits two different regimes of transport that intersect near 60 °C, the T_β of the hydrophilic sidechains. The values at 80 °C and 95 %RH are remarkably high, 0.228 and 0.298 S cm^{-1} for the PolyHPA-70 and PolyHPA-75, respectively. This high conductivity is achieved due the super acidic, and thus highly mobile, nature of the protons of silicotungstic acid. At lower temperatures, the energy barrier for transport is over 4 times greater than when compared to above 60 °C. This conductivity should enable high performance, practical devices and contributes to the low in-situ area specific resistances, discussed below.

The polymer's morphology was investigated using FIB / TEM under vacuum and SAXS under conditions relevant to fuel cell operation (elevated temperature and humidity). We first consider the SAXS equilibrated in air.

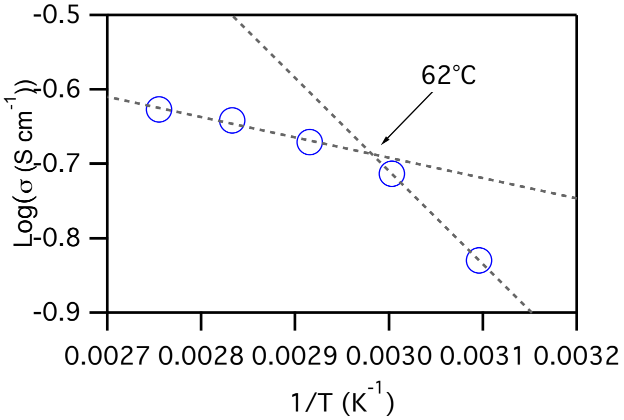

Figure 36: In-plane conductivity of PolyHPA-70 at 95 %RH and various temperatures with trend lines to guide the eye.

Two peaks appear in the SAXS, one at 0.097 and the other at 0.6 $Å^{-1}$ corresponding to d-spacing values of 6.5 and 1.0 nm (Figure 37a). The 1.0 nm feature is likely the spacing between two adjacent HSiW molecules and the 6.5 nm feature is likely the spacing between HSiW rich and deficient domains.

Examination of the high q peak, Figure 37b, shows a shift to lower q, or larger d-spacing that is highly dependent on RH. This is indicative of water moving towards the surface of the HSiW moieties and pushing them further apart. Interestingly with this system of HSiW and PolyPPA, this same SAXS pattern predominates whenever the material is processed. This strongly implies that a thermodynamic minimum is achieved with clusters of HSiW separated by a characteristic length of ca. 6.5 nm.

Looking at the TEM (Figure 37c) it appears as if two levels of clustering exist. First, there are three large clusters, which are at an irregular distance from each other, and therefore no d-spacing is observed in the SAXS data. On further investigation, many 3-4 nm clusters appear which are separated by a darker phase. The center to center distance of these smaller clusters is assigned to the 6.5 nm peak seen in the SAXS data. Bright spots in the TEM backscatter micrograph indicate regions with more heavy elements and from the EDS measurements (Figure 38), it is clear that the heaviest element in high concentration is W, therefore the bright spots must represent a phase enriched in W. A drastic change is noted in the scattering pattern of the liquid soaked film, Figure 37a. This change is likely a change from scattering dominated by structure factor scattering to a spectra dominated by form factor scattering, as indicated by the loss in peaks and drop in intensity.[69], [70], [71] We are now able to observe several radii of gyration (R_g) with values of 10, 4.2, and 1.3 nm. The feature with an R_g of 10 nm is assigned to the large bright clusters in Figure 37c while the feature with an R_g of 4.2 nm is assigned to the clusters that are separated by 6.5 nm at lower water contents. Lastly, the feature with a 1.3 nm R_g is assigned to the individual, solvated HSiW moieties.

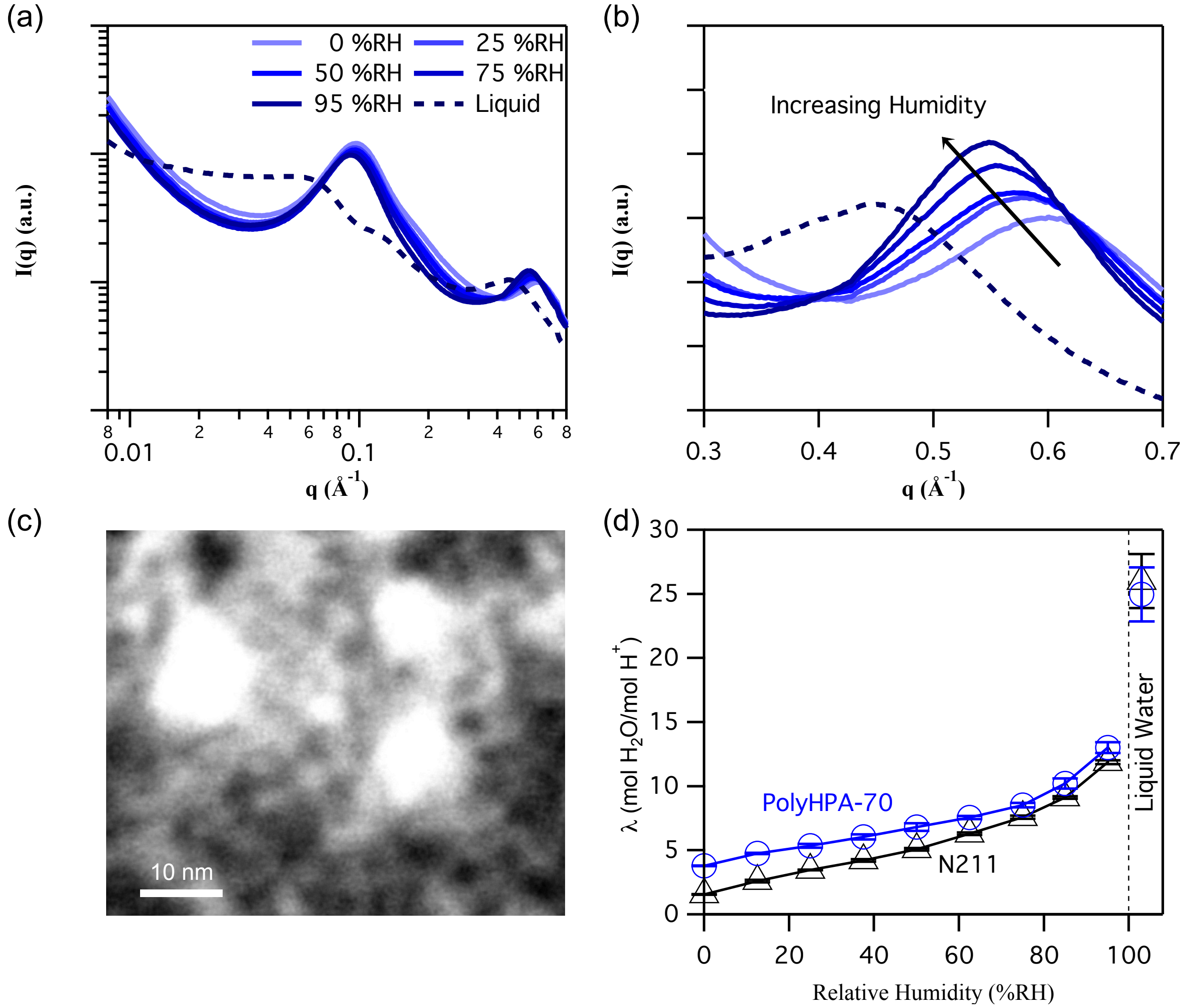

Figure 37: (a) SAXS at 80 °C in air at various humidities and in liquid water (b) High q region of the SAXS (c) TEM darkfield micrograph of PolyHPA-70 that was milled out from the bulk of the film using FIB (d) lambda vs. relative humidity for Nafion (Δ) and PolyHPA-70 (O) at 60°C

It is hypothesizes that increasing the continunity of the HSiW phase would serve to further improve the transport properties of the PolyHPA material. As compared to the Nafion® standard the water content in the film, more water per protogenic group is present at all humidities (See Figure 37d). The difference is most dramatic at low humidities where the highly hydroscopic nature of the HSiW causes retention of 3.79 H_2O/H^+ (15.1 per HSiW) in dry N_2 at 60 °C, as determined by TGA, compared to 1.55 for Nafion®.[72] In liquid water the PolyHPA-70 has a similar λ as nafion, but its swelling behaviour is different. The dimensional swelling of N211 was measured at $\Delta z = 2\pm2\%$ and $\Delta x\text{-}y = 32\pm7\%$ in contrast, the PolyHPA-70 film dimensional swelling was $\Delta z = 24\pm5\%$ and $\Delta x\text{-}y = 56\pm5\%$.

As the film is humidified and the water content increases, the 1 nm peak shifts to lower q and thus higher d-spacing. This is not true for the 6.5 nm peak and is an indication that more water is not hydrating the HSiW in the 6.5 nm peak until the film is immersed in liquid water.

Chemical and Mechanical Stability of 80 µm films: This material has been designed to solve the chemical stability issues discussed in the introduction through incorporation of a large amount of HSiW (a radical decomposition catalyst) into a polymer film. To probe the chemical and mechanical stability of these materials, ASTs, based on U.S. Department of Energy (DOE) suggested protocols, were performed.[73], [74], [75] Several PolyHPA-70 (80 µm) films were used for preliminary testing. The first film easily passed the mechanical AST with <1 mA cm^{-2} hydrogen crossover after 22,500 wet dry cycles (LSV can be seen in Figure 39a) which has been previously reported.[53] This particular MEA was fabricated using a CCM and the fuel cell performance was rather poor given the high proton conductivity. The end of life fuel cell performance is shown in Figure 38.

Once these films were made, the initial interest was mechanical and chemical stability. Two films were tested in the chemical stability test and one was tested in the mechanical stability test. The fuel cell that was tested in the mechanical stability test was fabricated using a CCM method and while it passed the mechanical AST, the fuel cell performance was very poor. The rest of the PolyHPA fuel cells were made using commercial GDEs and showed much greater performance, see Figure 40 in the main text. The end of life performance for the fuel cell that passed the mechanical AST can be seen in Figure 38

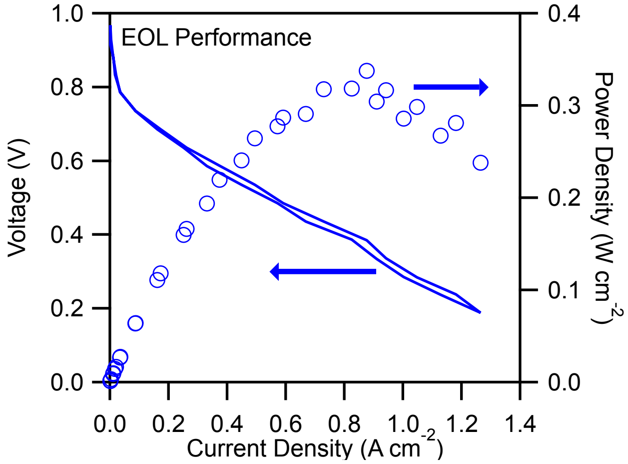

Figure 38 Data from Mechanical AST that was conducted on an 80 µm film with each cycle consisting of 30 second dry / 30 second wet N_2 flow the polarization data collected after 22,500 cycles at 80°C/100%RH.

The rest of the fuel cells were fabricated using commercial GDEs, which resulted in much greater performance, see below. While this is an achievement, films with mechanical supported are often able to easily pass this AST and this problem is considered solved by many in the community. The challenge that motivated this research was making a film that was highly chemically stable. To test the hypothetical chemical stability of this material, a chemical AST was performed at 90 °C, 30 %RH, under an H2-O2 environment at OCV. Under these conditions, standard polymer electrolyte membranes degrade rapidly, this is due to radical generation and subsequent attack of the polymer film. It has been previously demonstrated that the decay is much more rapid under an O2 environment, as used here, as opposed to air, the standard DOE protocol.[76] Under O2 during this test Pt has been shown to dissolve and precipitate as a Pt band in the membrane, this phenomenon is also seen in real fuel cells that are cycled through OCV. The accelerated degradation, in the AST using O2, has been attributed to decomposition of the PFSA polymer near the Pt band, which is more prevalent in O_2 environments.[77] Below in Figure 39b is the OCV vs. time for two different batches of PolyHPA-70 (80 µm) and a Nafion® 211 control.

This remarkably low OCV decay (100 µV hr-1), without OCV recovery, and under very harsh conditions represents the lowest rate reported to date in the literature.[78]

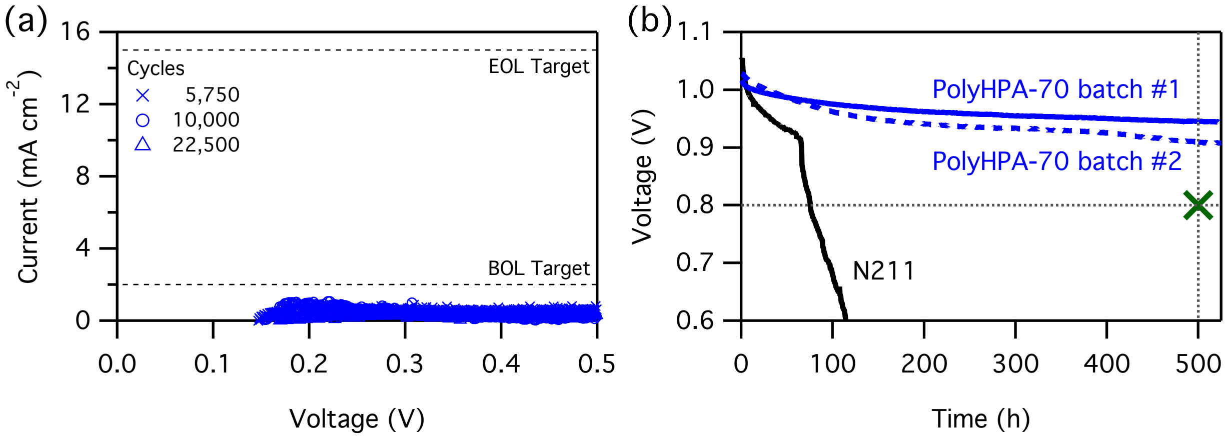

Figure 39: (a) LSV for PolyHPA-70 (80 µm) after wet/dry cycling and beginning of life and end of life crossover targets (b) OCV hold test at 90 °C/ 30 %RH under H_2-O_2 flow and no current. Two different batches of PolyHPA-70 (80 µm) easily pass the test while N211 film for comparison (bottom trace). The typical target is 500 h while retaining a voltage above 0.8 V which is marked (x).

This accomplishment is particularly remarkable because the HSiW acts as both the proton conducting moiety and the radical decomposition catalyst allowing for high performance with a highly chemically and mechanically stable material.

Fuel Cell Performance: In addition to the chemical stability, this material was designed to have exceptional H^+ transport properties, as HPAs are some of the most conductive solids known due to their highly delocalized negative charge, as stated in the introduction. A 48 µm film of PolyHPA-70 and a 20 µm film of PolyHPA-75 were used to fabricate fuel cells where the films had 70 and 75 theoretical wt% HSiW loadings, respectively. The performance under a H_2-O_2 and H_2-air environments were evaluated, and compared with an MEA constructed from N211 and standard electrodes optimized for N211. The PolyHPA fuel cells do not utilize optimized electrodes and the testing presented here is used solely to evaluate the PolyHPA membranes and are not to be taken as the performance of a future optimized fuel cell, using these materials. In fact, this is evident from the mass transfer limitations observed under H2-air operation.

The I-V performance of the PolyHPA-75, PolyHPA-70 and N211 under saturated inlet gasses at 80 °C and different oxidants can be seen in Figure 40a. The performance of both PolyHPA-75 and PolyHPA-70 are very similar to the performance of N211, with the PolyHPA-75 fuel cell out performing N211 at higher current densities.

Using a very simple fuel cell model, this data was fit to further analyse the contributions to the overpotential losses by kinetic, ohmic, and transport factors.[79], [80] The equation used to for the model was:

$$V(i) = E_{OCV} - b\log\left(\frac{i}{i_0}\right) - iR_{hf} + a\log\left(1 - \frac{i}{i_{lim}}\right) \quad [1]$$

where V(i) is the voltage as a function of i (current), EOCV is the open circuit voltage, a and b are fitting parameters and i0, Rhf, and ilim are the exchange current density, HFR, and limiting current density, respectively. The kinetic, ohmic, and transport losses are the second, third, and forth terms on the right hand side of equation 1, respectively. The ohmic losses can be seen in Figure 40b. For PolyHPA-75, a 22 % reduction in HFR at 2 A cm^{-2} results in less ohmic losses than PolyHPA-70, which has nearly the same ohmic losses as the optimized N211 cell. This is remarkable considering that the PolyHPA-70 fuel cell is 48 μm compared to the thinner N211 which is 25 μm. The kinetic losses (see Figure 40c) are slightly better for the optimized N211 fuel cell made with a CCM than for the PolyHPA fuel cells fabricated using commercial GDEs. The last source of losses considered in this model is derived from transport losses (see Figure 40d) and is the cause of poor fuel cell performance in air. To fully take advantage of the PolyHPA, the membrane / electrode interface needs to be optimized and the transport losses in air need to be minimized.

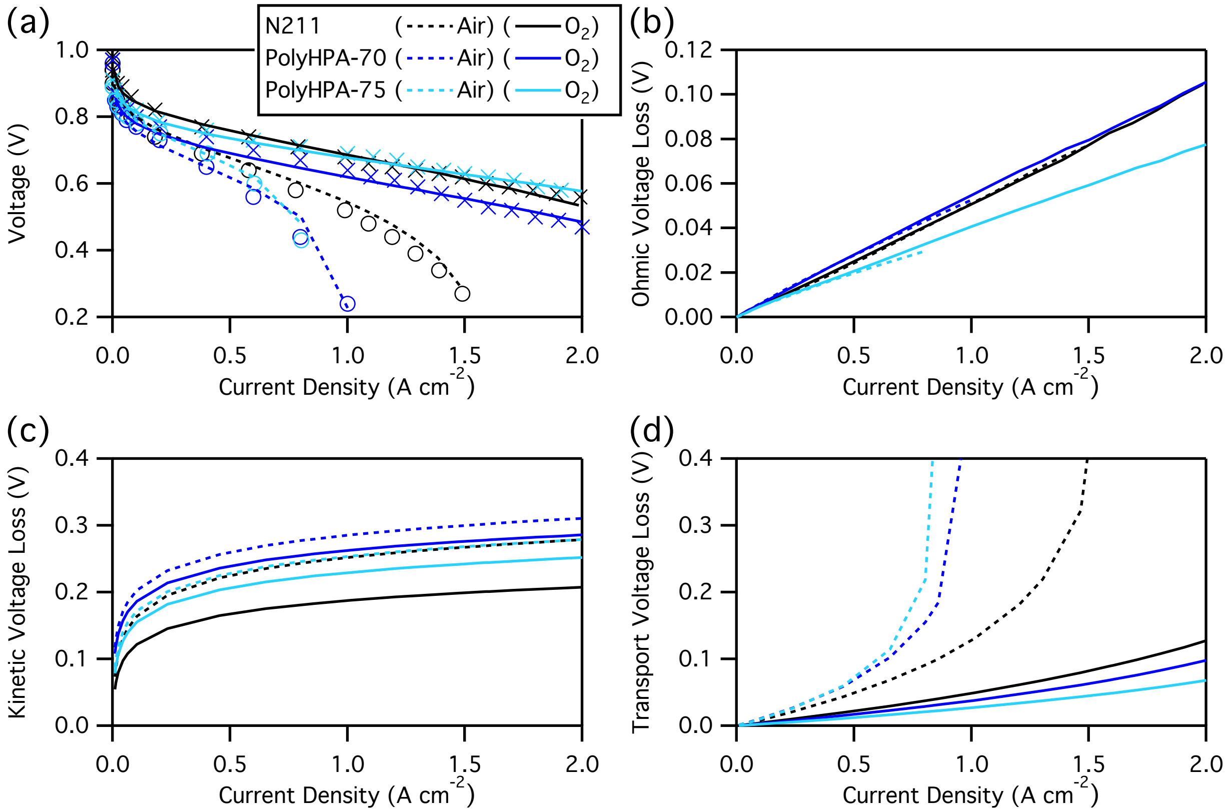

Figure 40: (a) I-V data for N211 (25 μm), PolyHPA-70 (48 μm), and PolyHPA-75 (20 μm) at 80 °C and saturated inlet gases with both air (O) and O$_2$ (X). Experimental data are markers and simulated data is the line, as indicated in the legend. The simulated ohmic (b), kinetic (c), and transport (d) voltage losses vs. current density.

Next, the PolyHPA-70 fuel cell was evaluated under low humidity operation at 80 °C, see Figure 41. A drop in voltage and an increase in HFR is seen, as expected. At low current densities the HFR starts out near 1000 mΩ cm^2, but drops to 141 mΩ cm^2 at 2 A cm^{-2}. This HFR drop can be attributed to increase in water generation from increasing current densities. Looking at the HFR values at low current density, an order of magnitude increase occurs when the humidity is reduced from 100 to 50 %RH, indicative of poor transport under low RH.

The transport rate of H_2 in the device are similar to N211. The H_2 crossover, normalized for thickness, is slightly higher for PolyHPA-70 (0.69 μmol cm^{-2} hr^{-1}) than for N211 (0.56 μmol m^{-2} hr^{-1}) at 80 °C. Two routes for improving chemical stability are reducing the crossover of H_2 and adding a radical decomposition catalyst. Due to the similar H_2 crossover values, it can be concluded that the HSiW is indeed acting as a radical decomposition catalyst. The H_2O transport rate in PolyHPA-70 is double that of N211 (0.55, and 1.10 μmol cm^{-1} hr^{-1}, respectively). All of the species transport data (see Figure 42) have been normalized for film thickness to provide a fair comparison.

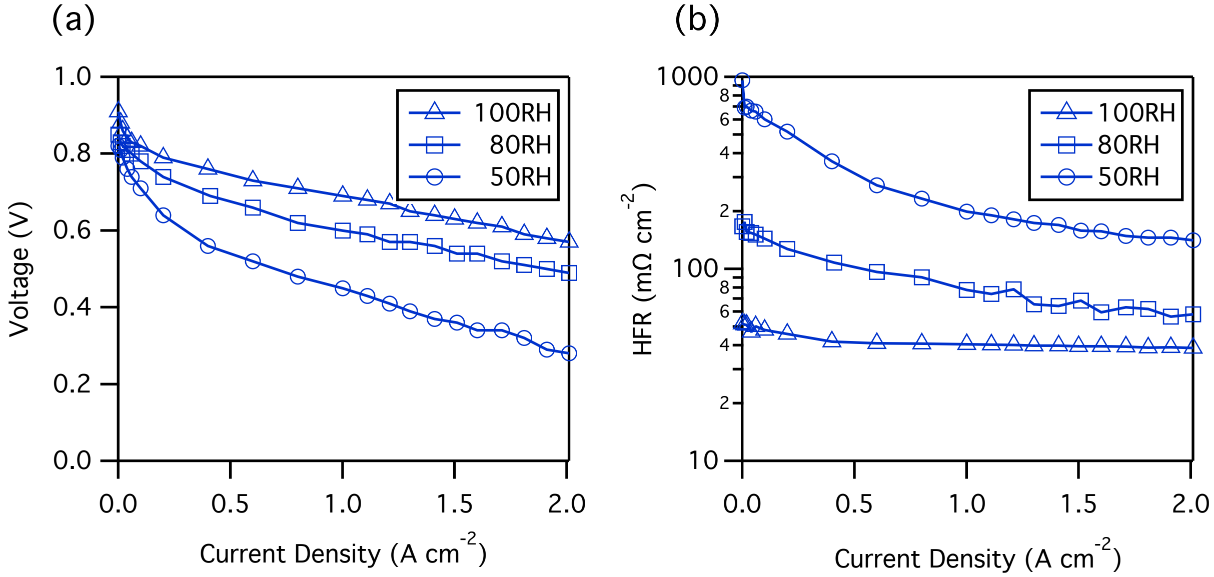

Figure 41: PolyHPA-75 voltage (a) and HFR (b) at different humidities vs. current at 80°C.

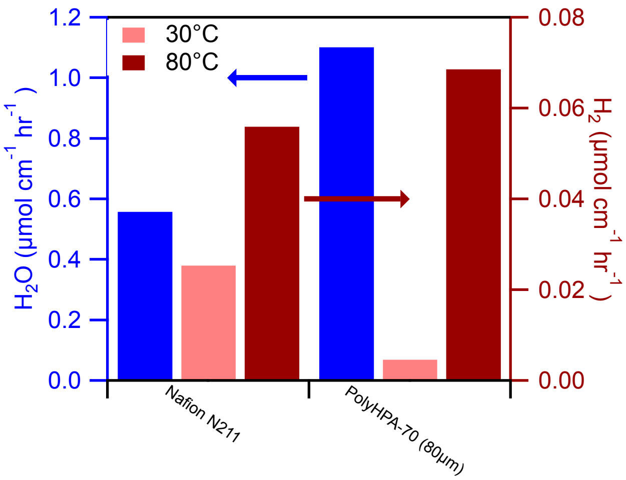

Figure 42: Species transport in MEA for N211, and two different PolyHPA-70 films. The H_2 transport rates were measured at 100 %RH. All values are normalized by thickness.

The rapid water transport rate is important, allowing for rapid diffusion of water from the cathode to the anode even with thicker films, which reduces the need for external humidification.

<u>Chemical Stability of a 30 μm film in a 50 cm^2 MEA: </u>At this point, a 50 cm^2 MEA using a 30 μm PolyHPA-70 film was prepared to better align with the DOE membrane targets and tested at NREL. The goal of this test was to ensure the chemical stability was sufficient even with thinner films where H_2 crossover is higher and chemical stability is lowered. This was the first MEA of this size and the performance was worse than the smaller fuel cells with films of similar thickness and membrane composition. This is mainly attributed to a high interface resistance between the PolyHPA-70 membrane and the Nafion GDEs. See the polarization data in Figure 43 compared to the data in Figure 40.

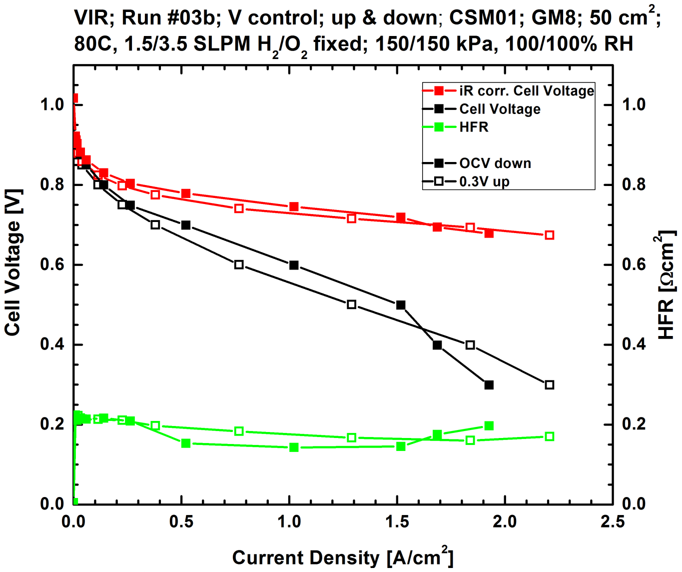

Figure 43: I-V data for the 50 cm^2 fuel cell fabricated using a 30 μm PolyHPA-70 film.

The HFR at 80 °C and saturated gasses (*ca.* 200 mΩ cm^2) is much higher than would be expected with a PolyHPA-70 membrane that is 30 μm thick. This is attributed to the need to optimize the fuel cell design for this new material and should not affect the chemical stability. After the preliminary data collection in a H_2-O_2 environment, a standard OCV hold in H_2-air at 90°C and 30 %RH was performed with hydrogen crossover measurements at 20-72 h intervals. After 500 h, the OCV had dropped to 0.72 V, see Figure 44.

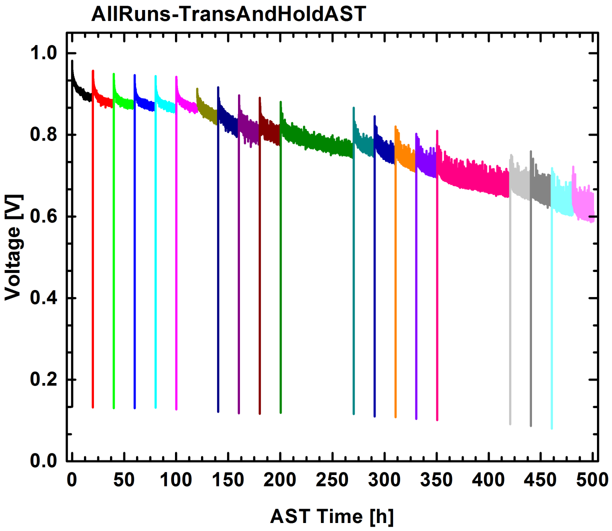

Figure 44: OCV vs time for the length for the AST

After the OCV hold is resumed after the LSV test is completed, the voltage spikes. This can be attributed to conversion of Pt-O to a more pristine Pt surface. The general trend is decreasing OCV with time. If all of the data is lined up starting with each testing window between LSV tests, the decay is consistent, see Figure 45.

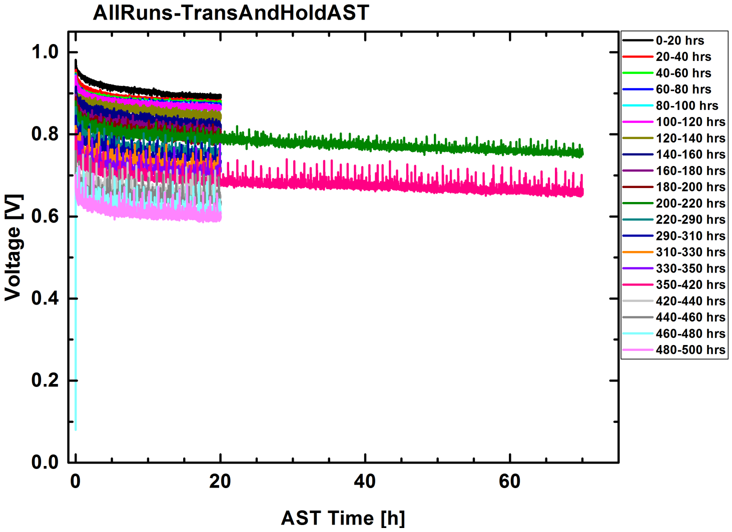

Figure 45: OCV hold vs. experiment time.

To further probe what is causing the loss in voltage, the LSV test was analyzed at a voltage of 0.4 V and the current vs. OCV hold time can be seen below in Figure 46. It appears as if two regimes exist. First, the current is constant at around 2 mA cm^{-2} for the first *ca.* 200 h and then there is a rise thereafter.

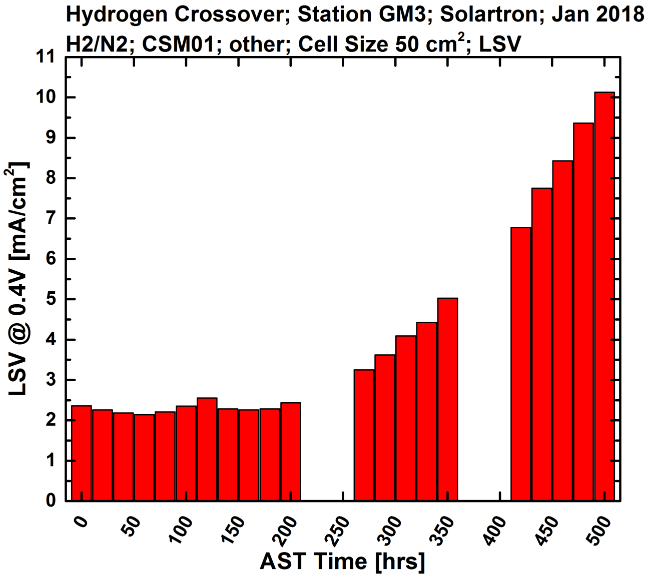

Figure 46: Current at 0.4 V at different points in the AST.

Even more insight can be gained through deconvolution of the different sources of current (electric short and hydrogen crossover). Hydrogen crossover will have a limiting current where the current reaches a plateau and does not increase with increasing current. This is not true of electric shorts. The slope between 0.25 and 0.50 V was used to calculate the contribution from electric shorts and then subtracted to create an artificial data set, which was then used to calculate the H_2 crossover. This analysis gave reasonable results initially, but towards the end of the OCV hold started to give nonsensical results, see Figure 47.

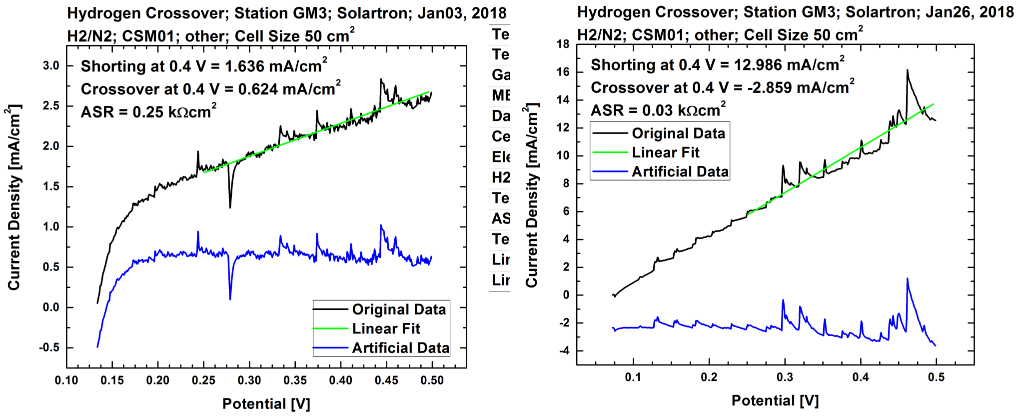

Figure 47: LSV data for a sample early in the OCV hold (left) and late in the OCV hold (right).

The slope used to calculate the electrical shortage was much higher later in the test and resulted in negative values for the artificial, H_2 crossover only current. While the H2 crossover values are not reliable, what is clear is the electric short current increases with OCV hold test time and can be attributed to the drop in OCV, not an issue with H_2 crossover. The membranes are not mechanically supported and likely suffer from thinning under high compression. Mechanical support must be investigated in the future to stop membrane thinning and electrical shorting.

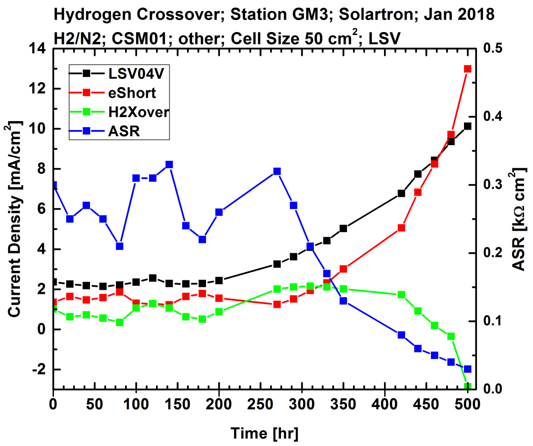

Figure 48: Crossover from LSV for different types of crossover.

7.4 Conclusions

This study has outlined the synthesis of a new material designed to have superior chemical stability and conductivity over PFSA polymer membranes, the current state of the art material. The PolyHPA material is made through attachment of phenol phosphonate ester sidechains to a commercial fluoroelastomer (FC-2178). These sidechains are subsequently converted into the phosphonic acid analogue through a hydrolysis step, yielding PolyPPA. Next, the PolyPPA is reacted with HSiW forming covalent bonds, immobilizing the HSiW.

Both IR and NMR (^{1}H, ^{19}F, ^{31}P) confirm the synthesis of a new material. SAXS and FIB/TEM indicate that the HSiW are clustering, which is hypothesized to be reducing the H^+ transport under low water content due to the non-continuous nature of these clusters. Even so, we have achieved very high proton conductivities of 0.228 and 0.298 S cm^{-1} for the PolyHPA-70 and PolyHPA-75, respectively, when humidified (80 °C and 95 %RH). This material offers a true shift in paradigm on chemical degradation mitigation. All previous strategies have used radical scavenging moieties that are not covalently bound to the polymer backbone and are free to migrate or potentially leach out of the film. In addition to this huge shortcoming of other approaches, most additives do not contribute to proton conductivity and addition of too much will lead to performance losses. Our method overcomes these challenges and resulted in outstanding chemical stability under chemical ASTs with a demonstrated OCV decay rate of 100 $\mu V\ hr^{-1}$ under a H_2-O_2 environment. Additionally, the HFR is 22 % lower in our films than in Nafion. Future work is needed to fully understand the relationship between the morphology and proton transport as well as to develop optimized electrodes for this fuel cell system. Additionally, making thin (ca. 10 μm) composite films with mechanical support would further improve fuel cell performance. Incorporation of different HPA moieties into this polymer system is also being investigated. This initial study highlights the potential for this PolyHPA platform to be integrated into a durable, high performance fuel cell.

References

(1) Schlichting, G. J.; Horan, J. L.; Jessop, J. D.; Nelson, S. E.; Seifert, S.; Yang, Y.; Herring, A. M. *Macromolecules* **2012**, *45*, 3874.

(2) Horan, J.; Genupur, A.; Ren, H.; Sikora, B.; Kuo, M.; Meng, F.; Dec, S.; Haugen, G.; Yandrasits, M.; Hamrock, S.; Frey, M.; Herring, A. *ChemSusChem* **2009**, *2*, 226.

(3) Horan, J. L.; Lingutla, A.; Ren, H.; Kuo, M.-C.; Sachdeva, S.; Yang, Y.; Seifert, S.; Greenlee, L. F.; Yandrasits, M. A.; Hamrock, S. J.; Frey, M. H.; Herring, A. M. *The Journal of Physical Chemistry C* **2014**, *118*, 135.

(4) Smith, D. W.; Babb, D. A. *Macromolecules* **1996**, *29*, 852.

(5) Choi, W.-S.; Harris, F. W. *Polymer* **2000**, *41*, 6213.

(6) Lee, K.-S.; Kim, J.-P.; Song, H.-S.; Jang, W.-G.; Park, Y.-S.; Lee, J.-S. *Macromolecular Rapid Communications* **2006**, *27*, 1330.

(7) Chandan, A.; Hattenberger, M.; El-Kharouf, A.; Du, S. F.; Dhir, A.; Self, V.; Pollet, B. G.; Ingram, A.; Bujalski, W. *Journal of Power Sources* **2013**, *231*, 264.

(8) Horan, J. L.; Lingutla, A.; Ren, H.; Kuo, M. C.; Sachdeva, S.; Yang, Y.; Seifert, S.; Greenlee, L. F.; Yandrasits, M. A.; Hamrock, S. J.; Frey, M. H.; Herring, A. M. *Journal of Physical Chemistry C* **2014**, *118*, 135.

(9) Herring, A. M. *Journal of Macromolecular Science, Part C: Polymer Reviews* **2006**, *46*, 245.

(10) Lejeune, N.; Dez, I.; Jaffrès, P.-A.; Lohier, J.-F.; Madec, P.-J.; Sopkova-de Oliveira Santos, J. *European Journal of Inorganic Chemistry* **2008**, *2008*, 138.

(11) Liu, Y.; Horan, J. L.; Schlichting, G. J.; Caire, B. R.; Liberatore, M. W.; Hamrock, S. J.; Haugen, G. M.; Yandrasits, M. A.; Seifert, S.; Herring, A. M. *Macromolecules* **2012**, *45*, 7495.

(12) Kim, G. S.; Hagen, K. S.; Hill, C. L. *Inorganic Chemistry* **1992**, *31*, 5316.

(13) Mayer, C. R.; Herson, P.; Thouvenot, R. *Inorganic Chemistry* **1999**, *38*, 6152.

(14) Klingele, M.; Breitwieser, M.; Zengerle, R.; Thiele, S. *J. Mater. Chem. A* **2015**, *3*, 11239.

(15) Motz, A. R.; Horan, J. L.; Kuo, M. C.; Herring, A. M. *ECS Transactions* **2015**, *69*, 587.

(16) Springer, T. E., Zawodzinski, T. A., Gottesfeld, S. *Journal of The Electrochemical Society* **1991**, *138*, 2334.

(17) Kongkanand, A.; Mathias, M. F. *J Phys Chem Lett* **2016**, *7*, 1127.

(18) Kundu, S.; Fowler, M. W.; Simon, L. C.; Grot, S. *Journal of Power Sources* **2006**, *157*, 650.

(19) Borup, R.; Meyers, J.; Pivovar, B.; Kim, Y. S.; Mukundan, R.; Garland, N.; Myers, D.; Wilson, M.; Garzon, F.; Wood, D.; Zelenay, P.; More, K.; Stroh, K.; Zawodzinski, T.; Boncella, J.; McGrath, J. E.; Inaba, M.; Miyatake, K.; Hori, M.; Ota, K.; Ogumi, Z.; Miyata, S.; Nishikata, A.; Siroma, Z.; Uchimoto, Y.; Yasuda, K.; Kimijima, K.; Iwashita, N. *Chem Rev* **2007**, *107*, 3904.

(20) Kusoglu, A.; Weber, A. Z. *J Phys Chem Lett* **2015**, *6*, 4547.

(21) Kusoglu, A.; Weber, A. Z. *Chem Rev* **2017**, *117*, 987.

(22) Tang, Y.; Kusoglu, A.; Karlsson, A. M.; Santare, M. H.; Cleghorn, S.; Johnson, W. B. *Journal of Power Sources* **2008**, *175*, 817.

(23) Zatoń, M.; Rozière, J.; Jones, D. J. *Sustainable Energy Fuels* **2017**, *1*, 409.

(24) Lee, S. Y.; Shin, D. W.; Wang, C.; Lee, K. H.; Guiver, M. D.; Lee, Y. M. *Electrochemistry Communications* **2013**, *31*, 120.

(25) Shi, Z.; Holdcroft, S. *Macromolecules* **2005**, *38*, 4193.

(26) Lee, S. Y.; Kang, N. R.; Shin, D. W.; Lee, C. H.; Lee, K.-S.; Guiver, M. D.; Li, N.; Lee, Y. M. *Energy & Environmental Science* **2012**, *5*, 9795.

(27) Li, N.; Lee, S. Y.; Liu, Y.-L.; Lee, Y. M.; Guiver, M. D. *Energy Environ. Sci.* **2012**, *5*, 5346.

(28) Park, C. H.; Lee, S. Y.; Hwang, D. S.; Shin, D. W.; Cho, D. H.; Lee, K. H.; Kim, T. W.; Kim, T. W.; Lee, M.; Kim, D. S.; Doherty, C. M.; Thornton, A. W.; Hill, A. J.; Guiver, M. D.; Lee, Y. M. *Nature* **2016**, *532*, 480.

(29) Curtin, D. E.; Lousenberg, R. D.; Henry, T. J.; Tangeman, P. C.; Tisack, M. E. *Journal of Power Sources* **2004**, *131*, 41.

(30) Gittleman, C. S.; Coms, F. D.; Lai, Y.-H. **2012**, 15.

(31) Gubler, L.; Koppenol, W. H. *Journal of The Electrochemical Society* **2012**, *159*, B211.

(32) Trogadas, P.; Parrondo, J.; Ramani, V. *Electrochemical and Solid-State Letters* **2008**, *11*, B113.

(33) Banham, D.; Ye, S.; Knights, S.; Stewart, S. M.; Wilson, M.; Garzon, F. *Journal of Power Sources* **2015**, *281*, 238.

(34) Baker, A. M.; Mukundan, R.; Spernjak, D.; Judge, E. J.; Advani, S. G.; Prasad, A. K.; Borup, R. L. *Journal of The Electrochemical Society* **2016**, *163*, F1023.

(35) Baker, A. M.; Babu, S. K.; Mukundan, R.; Advani, S. G.; Prasad, A. K.; Spernjak, D.; Borup, R. L. *Journal of The Electrochemical Society* **2017**, *164*, F1272.

(36) Baker, Andrew M.; Williams, S. T. D.; Mukundan, R.; Spernjak, D.; Advani, S. G.; Prasad, A. K.; Borup, R. L. *J. Mater. Chem. A* **2017**, *5*, 15073.

(37) Ramani, V.; Kunz, H. R.; Fenton, J. M. *Electrochimica Acta* **2005**, *50*, 1181.

(38) Haugen, G. M.; Meng, F.; Aieta, N. V.; Horan, J. L.; Kuo, M.-C.; Frey, M. H.; Hamrock, S. J.; Herring, A. M. *Electrochemical and Solid-State Letters* **2007**, *10*, B51.

(39) Paul Brooker, R.; Bonville, L. J.; Slattery, D. K. *Journal of the Electrochemical Society* **2012**, *160*, F75.

(40) Duncan, D. C.; Chambers, R. C.; Hecht, E.; Hill, C. L. *Journal of the American Chemical Society* **1995**, *117*, 681.

(41) Chen, D.; Xue, Z.; Su, Z. *Journal of Molecular Catalysis A: Chemical* **2004**, *208*, 91.

(42) Kamata, K.; Yonehara, K.; Sumida, Y.; Yamaguchi, K.; Hikichi, S.; Mizuno, N. *Science* **2003**, *300*, 964.

(43) Rowshanzamir, S.; Peighambardoust, S. J.; Parnian, M. J.; Amirkhanlou, G. R.; Rahnavard, A. *International Journal of Hydrogen Energy* **2015**, *40*, 549.

(44) Zhang, B.; Cao, Y.; Li, Z.; Wu, H.; Yin, Y.; Cao, L.; He, X.; Jiang, Z. *Electrochimica Acta* **2017**, *240*, 186.

(45) Malers, J. L.; Sweikart, M.-A.; Horan, J. L.; Turner, J. A.; Herring, A. M. *Journal of Power Sources* **2007**, *172*, 83.

(46) Rhoden, S. L. N. H.; Linkous, C. A.; Mohajeri, N.; Díaz, D. J.; Brooker, P.; Slattery, D. K.; Fenton, J. M. *Journal of The Electrochemical Society* **2010**, *157*, B1095.

(47) Hasani-Sadrabadi, M. M.; Dashtimoghadam, E.; Majedi, F. S.; Moaddel, H.; Bertsch, A.; Renaud, P. *Nanoscale* **2013**, *5*, 11710.

(48) Hasani-Sadrabadi, M. M.; Dashtimoghadam, E.; Majedi, F. S.; VanDersarl, J. J.; Bertsch, A.; Renaud, P.; Jacob, K. I. *Nano Energy* **2016**, *23*, 114.

(49) Nakamura, O.; Kodama, T.; Ogino, I.; Miyake, Y. *Chemistry Letters* **1979**, 17.

(50) Lavrenčič Štangar, U.; Orel, B.; Vince, J.; Jovanovski, V.; Spreizer, H.; Šurca Vuk, A.; Hočevar, S. *Journal of Solid State Electrochemistry* **2004**, *9*, 106.

(51) Horan, J. L.; Genupur, A.; Ren, H.; Sikora, B. J.; Kuo, M.-C.; Meng, F.; Dec, S. F.; Haugen, G. M.; Yandrasits, M. A.; Hamrock, S. J.; Frey, M. H.; Herring, A. M. *ChemSusChem* **2009**, *2*, 193.

(52) Liu, Y.; Horan, J. L.; Schlichting, G. J.; Caire, B. R.; Liberatore, M. W.; Hamrock, S. J.; Haugen, G. M.; Yandrasits, M. A.; Seifert, S. n.; Herring, A. M. *Macromolecules* **2012**, *45*, 7495.

(53) Motz, A. R.; Kuo, M.-C.; Herring, A. M. *ECS Transactions* **2017**, *80*, 565.

(54) Taguet, A.; Ameduri, B.; Boutevin, B. *Fuel Cells* **2006**, *6*, 331.

(55) Taguet, A.; Ameduri, B.; Boutevin, B. *Advances in Polymer Science* **2005**, *184*, 127.

(56) Logothetis, A. L. *Progress in Polymer Science* **1989**, *14*, 251.

(57) Starkweather, H. W.; Ferguson, R. C.; Chase, D. B.; Minor, J. M. *Macromolecules* **1985**, *18*, 1684.

(58) Rocchiccioli-Deltcheff, C.; Fournier, M.; Franck, R.; Thouvenot, R. *Inorganic Chemistry* **1983**, *22*, 207.

(59) Förner, W.; Badawi, H. M. *Journal of Structural Chemistry* **2011**, *52*, 471.

(60) Taguet, A.; Ameduri, B.; Boutevin, B. *Journal of Polymer Science Part a-Polymer Chemistry* **2006**, *44*, 1855.

(61) Kobayashi, S.; Chow, T.; Kawabata, H.; Saegusa, T. *Polymer Bulletin* **1986**, *16*, 269.

(62) Ramani, V.; Kunz, H. R.; Fenton, J. M. *Journal of Membrane Science* **2004**, *232*, 31.

(63) Wang, D.-J.; Fang, Z.-D.; Wei, X.-H. *Chinese Journal of Chemistry* **2005**, *23*, 1600.

(64) Neelakandan, S.; Rana, D.; Matsuura, T.; Muthumeenal, A.; Kanagaraj, P.; Nagendran, A. *Solid State Ionics* **2014**, *268*, 35.

(65) Matsumoto, K. Y.; Sasaki, Y. *Bulletin of the Chemical Society of Japan* **1976**, *49*, 156.

(66) Niu, J.-Y.; Zhao, J.-W.; Wang, J.-P. *Inorganic Chemistry Communications* **2004**, *7*, 876.

(67) Janik, M. J.; Bardin, B. B.; Davis, R. J.; Neurock, M. *J Phys Chem B* **2006**, *110*, 4170.

(68) Jouannet, D.; Pham, T.-N.; Pimbert, S.; Levesque, G. *Polymer* **1997**, *38*, 5137.

(69) Pedersen, J. S. *Advances in Colloid and Interface Science* **1997**, *70*, 171.

(70) Strobl, G. R. *The Physics of Polymers: Concepts for Understanding Their Structures and Behavior*.

(71) Strobl, G. R.; Schneider, M. *Journal of Polymer Science: Polymer Physics Edition* **1980**, *18*, 1343.

(72) James, P. J.; Elliott, J. A.; McMaster, T. J.; Newton, J. M.; Elliott, A. M. S.; Hanna, S.; Miles, M. J. *Journal of Materials Science* **2000**, *35*, 5111.

(73) Inaba, M.; Kinumoto, T.; Kiriake, M.; Umebayashi, R.; Tasaka, A.; Ogumi, Z. *Electrochimica Acta* **2006**, *51*, 5746.

(74) Huang, X.; Solasi, R.; Zou, Y.; Feshler, M.; Reifsnider, K.; Condit, D.; Burlatsky, S.; Madden, T. *Journal of Polymer Science Part B: Polymer Physics* **2006**, *44*, 2346.

(75) Lai, Y.-H.; Mittelsteadt, C. K.; Gittleman, C. S.; Dillard, D. A. *Journal of Fuel Cell Science and Technology* **2009**, *6*, 021002.

(76) Ohma, A.; Suga, S.; Yamamoto, S.; Shinohara, K. *Journal of The Electrochemical Society* **2007**, *154*, B757.

(77) Ohma, A.; Yamamoto, S.; Shinohara, K. *Journal of Power Sources* **2008**, *182*, 39.

(78) Yadav, R.; DiLeo, G.; Dale, N.; Adjemian, K. *ECS Transactions* **2013**, *53*, 187.

(79) Weber, A. Z.; Borup, R. L.; Darling, R. M.; Das, P. K.; Dursch, T. J.; Gu, W.; Harvey, D.; Kusoglu, A.; Litster, S.; Mench, M. M.; Mukundan, R.; Owejan, J. P.; Pharoah, J. G.; Secanell, M.; Zenyuk, I. V. *Journal of the Electrochemical Society* **2014**, *161*, F1254.

(80) Pant, L. M.; Yang, Z.; Perry, M. L.; Weber, A. Z. *Journal of The Electrochemical Society* **2018**, *165*, F3007.